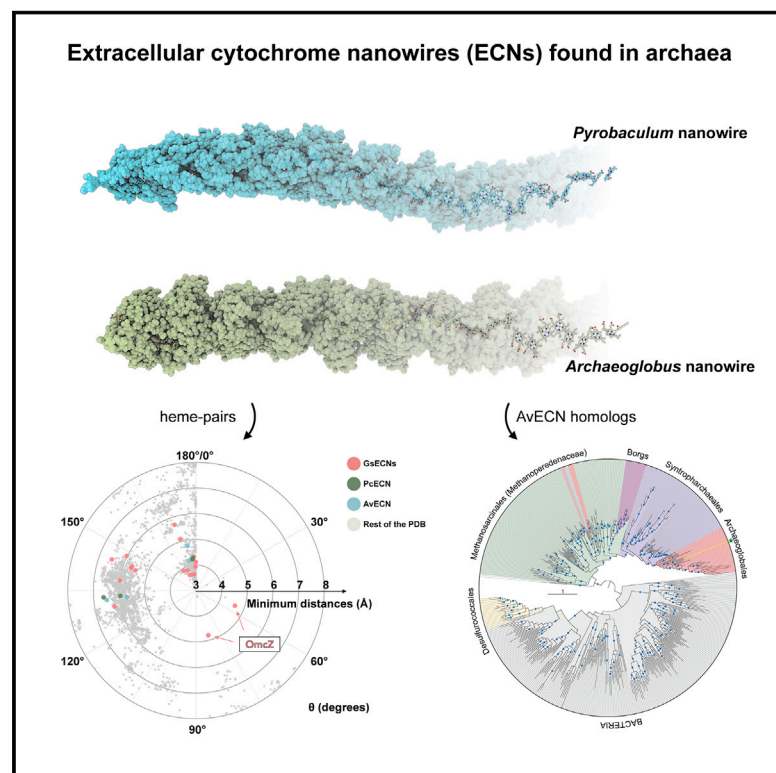# Cell

Extracellular cytochrome nanowires appear to be ubiquitous in prokaryotes

Graphical abstract

Authors

Diana P. Baquero,
Virginija Cvirkaite-Krupovic,
Shengen Shawn Hu, ...,
Edward H. Egelman, Mart Krupovic,
Fengbin Wang

Correspondence

egelman@virginia.edu (E.H.E.),
mart.krupovic@pasteur.fr (M.K.),
jerrywang@uab.edu (F.W.)

In brief

Heme organization, rather than protein structure, is conserved in nanowire cytochrome filaments from archaea and bacteria.

Highlights

- Atomic structures of extracellular cytochrome nanowires (ECNs) from archaea revealed

- Structurally unrelated bacterial and archaeal ECNs have the same heme stacking

- ECN homologs are widespread in archaea, including ANME-2, and Borg megaplasmids

- *Archaeoglobus veneficus* ECN may have evolved from c552-family cytochromes

CellPress

Cell

CellPress

Article

Extracellular cytochrome nanowires appear to be ubiquitous in prokaryotes

Diana P. Baquero,[1,6] Virginija Cvirkaite-Krupovic,[1,6] Shengen Shawn Hu,[2] Jessie Lynda Fields,[3] Xing Liu,[4] Christopher Rensing,[4] Edward H. Egelman,[2,*] Mart Krupovic,[1,*] and Fengbin Wang[2,3,5,7,*]

[1]Institut Pasteur, Université Paris Cité, CNRS UMR6047, Archaeal Virology Unit, Paris 75015, France
[2]Department of Biochemistry and Molecular Genetics, University of Virginia School of Medicine, Charlottesville, VA 22903, USA
[3]Department of Biochemistry and Molecular Genetics, University of Alabama at Birmingham, Birmingham, AL 35233, USA
[4]Fujian Provincial Key Laboratory of Soil Environmental Health and Regulation, College of Resources and Environment, Fujian Agriculture and Forestry University, Fuzhou 350002, Fujian, China
[5]O'Neal Comprehensive Cancer Center, University of Alabama at Birmingham, Birmingham, AL 35233, USA
[6]These authors contributed equally
[7]Lead contact
*Correspondence: egelman@virginia.edu (E.H.E.), mart.krupovic@pasteur.fr (M.K.), jerrywang@uab.edu (F.W.)
https://doi.org/10.1016/j.cell.2023.05.012

SUMMARY

Electrically conductive appendages from the anaerobic bacterium *Geobacter sulfurreducens*, recently identified as extracellular cytochrome nanowires (ECNs), have received wide attention due to numerous potential applications. However, whether other organisms employ similar ECNs for electron transfer remains unknown. Here, using cryoelectron microscopy, we describe the atomic structures of two ECNs from two major orders of hyperthermophilic archaea present in deep-sea hydrothermal vents and terrestrial hot springs. Homologs of *Archaeoglobus veneficus* ECN are widespread among mesophilic methane-oxidizing Methanoperedenaceae, alkane-degrading Syntrophoarchaeales archaea, and in the recently described megaplasmids called Borgs. The ECN protein subunits lack similarities in their folds; however, they share a common heme arrangement, suggesting an evolutionarily optimized heme packing for efficient electron transfer. The detection of ECNs in archaea suggests that filaments containing closely stacked hemes may be a common and widespread mechanism for long-range electron transfer in both prokaryotic domains of life.

INTRODUCTION

In anoxic environments, from aquatic sediments to the human gut, respiring bacteria naturally transfer electrons across micron-scale distances beyond their outer membranes to distant and insoluble terminal electron acceptors.[1–3] It is hypothesized that long-range electron transfer played an important role in microbial metabolism on the early earth, when iron as Fe(II) was the most accessible transition metal, with Fe(III) being a potential electron acceptor owing to the presence of small amounts of Fe(III) at low levels of oxygen.[4] Fe(III) could have been present as hematite or magnetite, necessitating the presence of extracellular nanowires so that the different Fe(III) compounds could be used as terminal electron acceptors. Other processes benefiting from bacterial nanowires include direct interspecies electron transfer (DIET), which paves the way for energetic coupling between different species in diverse anaerobic microbial communities.[5] For instance, recent reports indicated that nanowire-mediated DIET prevails in certain anaerobic digesters and can provide electrons for the reduction of CO_2 to CH_4.[6] Furthermore, microbial nanowire-mediated DIET has also been reported to contribute to the key environmental processes,

such as anaerobic oxidation of methane coupled to sulfate reduction,[7,8] anaerobic photosynthesis,[9] and anoxic, dark carbon fixation.[10] However, the molecular underpinnings of long-distance electron transfer have only been identified in the soil bacterium *Geobacter sulfurreducens*.[11]

G. sulfurreducens has been extensively studied as a model organism to understand the structure and function of conductive extracellular nanowires. The identity of the conductive filamentous appendages enabling extracellular electron transfer (EET) has been a topic of active debate.[11] With major technological advances in cryoelectron microscopy (cryo-EM)[12,13] the microbial nanowires in *G. sulfurreducens* have been shown to be polymerized filamentous extracellular cytochromes, containing either OmcS,[14,15] OmcE,[16] or OmcZ.[17] On the other hand, the notion that these extracellular filaments are 3-nm diameter "e-pili," containing only the N-terminal chain of the type IV pilin, PilA-N, has now been debunked with the determination of an actual structure for the PilA filament, showing that it is composed of two chains and is incompatible with electron transport.[16,18]

The multi-heme c-type cytochromes OmcS, OmcE, and OmcZ have protein structures that are ~80% loops, lacking extensive secondary structure and a conserved structural fold.

However, comparing the heme arrangements in the polymerized filaments, these three extracellular cytochrome nanowires (ECNs) fall into two different categories. OmcE and OmcS have very similar heme arrangements, and their hemes are insulated from solvent by a protein shield, consistent with a model where nanowires link a cell to a nearby metal oxide particle.[16] In contrast, OmcZ possesses an entirely different heme arrangement, with each subunit containing a branched solvent-exposed heme in addition to the linear chain of hemes so that networks of OmcZ filaments may form a conductive biofilm with a multiplicity of paths for electron flow.[17] With the large number of multi-heme cytochromes found in prokaryotic genomes, and the observed significant difference in heme arrangements, it is likely that conductive ECNs have arisen multiple times during evolution, and it was hypothesized that species other than *Geobacter sulfurreducens* could also produce ECNs.[11] Although multi-heme cytochromes encoded by methanotrophic archaea were predicted to mediate DIET,[7] no evidence of ECN existence outside of *G. sulfurreducens* has been presented thus far.

Here, we validate the hypothesis that ECNs are not restricted to *G. sulfurreducens* and discover such filaments in the second prokaryotic domain of life, the archaea. Using cryo-EM, we determined atomic structures of extracellular cytochrome filaments from two species of hyperthermophilic archaea, *Pyrobaculum calidifontis* and *Archaeoglobus veneficus*, belonging to two different phyla. Our observations suggest that ECNs may be ubiquitous in both prokaryotic domains and mediate long-range EET in diverse microbial communities.

RESULTS

Multi-heme c-type cytochrome filaments exist in archaeal strains

In archaea, genes encoding multi-heme c-type cytochrome were previously predicted in two major phyla, Euryarchaeota (orders *Archaeoglobales* and *Methanosarcinales*) and Crenarchaeota (orders *Thermoproteales* and *Desulfurococcales*).[19] To identify potential ECN candidates among the predicted multi-heme c-type cytochrome proteins, we applied the following filters that matched the expected features of ECNs: the proteins had to possess a predicted signal peptide, lack predicted transmembrane regions (outside of the signal peptide), be encoded with other multi-heme c-type cytochromes in the same strain, and lack sequence homology to an annotated enzyme fold. From a set of multi-heme c-type cytochromes that matched our criteria, for validation, we selected three ECN candidates from *P. calidifontis* (order *Thermoproteales*), *A. veneficus* (order *Archaeoglobales*), and *Methanolobus tindarius* (order *Methanosarcinales*). Cryo-EM analysis showed that *P. calidifontis* and *A. veneficus* each expressed an ECN: *P. calidifontis* ECN (PcECN) showed no obvious similarity to any previously determined protein fold; *A. veneficus* ECN (AvECN) also presented a new protein fold although distantly related to c552-family cytochromes (see below).
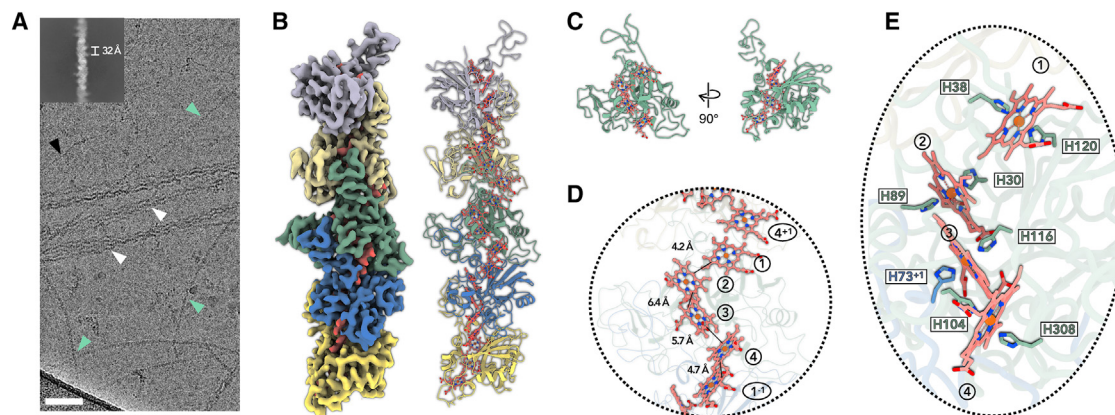
Cryo-EM of *P. calidifontis* ECN

We grew wild-type (WT) *P. calidifontis* (DSM 21063)[20] using sodium thiosulfate as the electron acceptor under microaerobic conditions. This environment promotes not only the production of cytochrome filaments but also other types of cell appendages, including biofilm-promoting TasA-like bundling filaments,[21] type IV pili, and conjugation pili (PDB: 8DFT). Images of ECN segments were easily separated from other types of filaments in reference-free 2D classifications. Unlike *Geobacter* OmcS filaments, PcECN does not display a sinusoidal morphology (Figure 1A). An averaged power spectrum from aligned raw particles shows a meridional layer line at ~1/(32 Å) and a layer line that can only be arising from a 1-start helix at ~1/(215 Å), establishing that there are ~6.6 subunits per turn of a ~215-Å-pitch 1-start helix (Figure S1; Table S1).

The final reconstruction reached 3.8-Å resolution with the application of helical symmetry. The 1-start helix was right handed, determined by the hand of α helices in the protein subunit, with a rise and rotation per subunit of 32.4 Å and 54.7°, respectively. The C_α tracing at such a resolution was straightforward, and after accounting for the protein density, the map showed that each ECN subunit contains four hemes. Finding the correct protein was unambiguous, as the *P. calidifontis* strain only encodes four proteins having more than two CxxCH heme-binding motifs: A3MW89 (four motifs), A3MW92 (three motifs), A3MW94 (eight motifs), and A3MW99 (eight motifs). Therein, A3MW94 and A3MW99 are excluded owing to the much larger number of predicted heme molecules per subunit. AlphaFold2[22] predictions of A3MW89 and A3MW92 were compared with the cryo-EM map. All side chains of A3MW92 agreed with the cryo-EM map. The presence of four hemes per subunit in the experimental map, but only three CxxCH heme-binding motifs in A3MW92, is explained by the filament model (see below). The AlphaFold2 prediction for A3MW89, the only protein having four heme-binding motifs, on the other hand, does not have an overall protein fold matching the cryo-EM map (Figure S2). Thus, A3MW92 was uniquely identified as the ECN protein in *P. calidifontis*. The model starts at position 24 of the predicted protein, suggesting that A3MW92 is N-terminally processed. Consistent with this observation, A3MW92 has a strongly predicted (p = 0.97) signal peptide[23] with a signal peptidase I cleavage site between positions Ala20 and Thr21 (Figures S3A and S3B). These results suggest that PcECN is externalized using the Sec secretion system.

Interestingly, the PcECN model has a considerably higher percentage of secondary structure content (15% α helices and 18% β strands; Figure 1C) compared with *G. sulfurreducens* ECNs: OmcS has 13% α helices and 6% β strands, OmcE has 19% α helices and 3% β strands, and OmcZ has 18% α helices and 4% β strands. We have previously shown that *G. sulfurreducens* ECNs do not have a conserved protein fold,[14,16,17] presumably because the key selection during evolution would be on maintaining the closely stacked heme arrangements, which would be possible without a conserved protein fold. We then asked whether PcECN has a structural fold similar to other known protein structures because its secondary structure content is ~10% higher. However, neither DALI[24] (distance matrix alignment) nor Foldseek[25] could identify a known experimentally determined structure having a similar fold, suggesting that PcECN has a fold never before seen in existing databases.

Figure 1. Cryo-EM of *P. calidifontis* ECN

(A) Cryo-EM image of cell appendages from *P. calidifontis* cells. Different species of filaments were observed and labeled correspondingly: PcECN (green arrowheads); archaeal bundling pili subunit, AbpA (white arrowheads); B-form DNA (black arrowhead). Scale bars, 50 nm. The upper left is a two-dimensional class average of the PcECN, showing the helical rise of 32 Å between adjacent subunits.

(B) The cryo-EM reconstruction (left) with backbone trace of the PcECN subunits (right). The heme molecules and their corresponding cryo-EM densities are shown in red. Each PcECN subunit is colored differently.

(C) The atomic model of one repeating subunit of PcECN. The protein backbone trace is green, and the heme molecules are shown in ball and stick representation in red.

(D) A close-up view of the filament to show the heme array in PcECN, with the minimum observed edge-to-edge distances indicated between adjacent porphyrin rings. Heme molecules are labeled with numbers in circles, "+1" and "−1" indicate protein subunits above and below the central subunit, respectively.

(E) The heme array in PcECN and the histidines coordinating these hemes. The histidines are colored by protein subunits using the same color scheme as in (B).

Despite having no protein fold similarity, the heme arrangements in the PcECN model are strikingly similar to those in the *G. sulfurreducens* OmcS and OmcE filaments. The neighboring heme porphyrin rings in the PcECN adopt either face-to-face antiparallel or T-shaped conformations, and those conformations take place alternately along the filament (Figures 1C and 1D). Furthermore, the edge-to-edge distances between porphyrin rings are comparable to OmcS and OmcE, ranging from 4.2 to 6.4 Å (Figure 1D), suggesting a similar electron transfer mechanism. In addition, similar to OmcS and OmcE, one heme (heme 3) per PcECN subunit is coordinated by H116 of the same subunit and H73 of an adjacent subunit (Figure 1E). Notably, the optimal growth condition for *P. calidifontis* is 90°C, significantly higher than that for *G. sulfurreducens* (30°C). The required extra thermostability of PcECN may be contributed by two intra-subunit disulfide bonds that were not observed in *G. sulfurreducens* ECNs (Figure S4). Furthermore, similar to other extracellular filaments of hyperthermophilic archaea, including type IV pili,[26,27] bundling pili[21] and flagella,[28] but unlike OmcS and OmcZ of *G. sulfurreducens*, PcECN appear to be glycosylated.

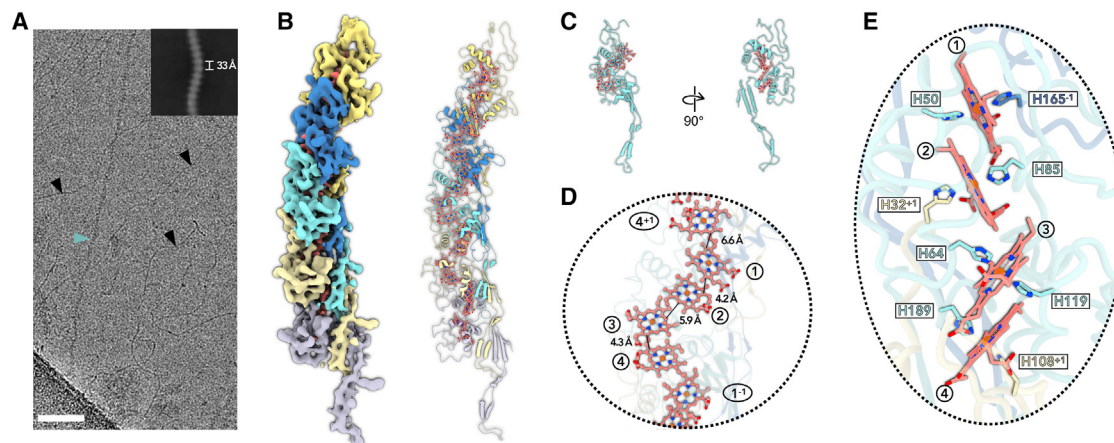## Cryo-EM of *A. veneficus* ECN

To obtain AvECNs, we grew WT *A. veneficus* cells (DSM 11195)[29] with sodium sulfite as the electron acceptor. Cryo-EM analysis of the AvECN (Figure 2) showed that the filament has a strong sinusoidal morphology with a pitch of ∼350 Å. An averaged power spectrum from aligned raw particles showed a meridional layer line at ∼1/(33 Å), establishing a helical rise of ∼33 Å and therefore a helical twist of ∼34°. After refining those parameters in the helical and subsequent non-uniform refine-

ment, a ∼4.1-Å-resolution reconstruction, judged by model:map Fourier shell correlation (FSC) (Table S1), was generated.

By tracing the protein chain, it was apparent that each AvECN subunit also contains four heme molecules (Figures 2B–2E), as was found for the PcECN. Interestingly, 17 proteins with three or more CxxCH motifs are present in the *A. veneficus* proteome. Among them, the AlphaFold predictions of only three, F2KMU7, F2KMU8, and F2KPF5, have a similar protein fold to the experimental chain trace and roughly agree with the cryo-EM map. After further investigation, F2KMU7 was excluded because it has a helix-rich region (residues 120–150) that cannot be explained by the cryo-EM map. Similarly, F2KPF5 was also excluded because it does not have enough residues to fit a loop region in the cryo-EM map (residues 131–151 in F2KPF5, whereas the corresponding loop in F2KMU8 contained residues 136–164). F2KMU8 can be fully built into the cryo-EM map and was therefore uniquely identified as the AvECN protein in *A. veneficus* (Figure S2). Similar to the PcECN, AvECN has a predicted N-terminal signal peptide[23] with the cleavage site located between Ser26 and Leu27 and is thus also likely transported across the membrane through the Sec secretion system (Figures S3C and S3D).

The AvECN has an even higher percentage of secondary structure content than PcECN, with 29% α helices and 15% β strands (Figure 2C). Strikingly, even with 44% of the residues in either α helices or β strands, DALI[24] and Foldseek[25] failed to identify a similar known experimentally determined protein fold. The AvECN fold was also unrelated to the fold of PcECN (Figure 1C). Within a single ECN subunit, four heme molecules are surrounded by a few sparsely distributed α helices. At the same time, the C-terminal region (residue 190–250) forms an extended "arm-like" architecture projecting out from the body

Figure 2. Cryo-EM of *A. veneficus* ECN

(A) Cryo-EM image of cell appendages from *A. veneficus* cells. Different filaments were observed and labeled correspondingly: AvECN (cyan arrowhead); B-form DNA (black arrowheads). Scale bars, 50 nm. The upper right is a two-dimensional class average of the AvECN filament, showing the helical rise of 33 Å between adjacent subunits.

(B) The cryo-EM reconstruction (left) with backbone trace of the AvECN subunits (right). The heme molecules and their corresponding cryo-EM densities are shown in red. Each AvECN subunit is colored differently.

(C) The atomic model of one repeating subunit of AvECN. The protein backbone trace is cyan, and the heme molecules are shown in ball and stick representation in red.

(D) A close-up view of the filament to show the heme array in AvECN, with the minimum observed edge-to-edge distances indicated between adjacent porphyrin rings. Heme molecules are labeled with numbers in circles, "+1" and "−1" indicate protein subunits above and below the central subunit, respectively.

(E) The heme array in AvECN and the histidine coordination of the hemes. The histidines are colored by protein subunits using the same color scheme as in (B) and (C).

of the subunit, composed of multiple antiparallel β strands (Figure 2C).

The stacking arrangements of heme porphyrin rings in AvECN are similar to those in PcECN and both the OmcS and OmcE filaments from *G. sulfurreducens*, in terms of edge-to-edge distances (Figure 2D) and alternately antiparallel and T-shaped stacking patterns. The most striking feature in AvECN relates to how heme molecules are coordinated: three out of four hemes in every AvECN subunit are coordinated by residues from two adjacent subunits: heme 1 is coordinated by H50 of the same subunit and H165 of the subunit above, heme 2 is coordinated by H85 of the same subunit and H32 of the subunit beneath, and heme 4 is coordinated by H189 of the same subunit and H108 of the subunit beneath (Figure 2E). This extensive heme sharing is not observed in bacterial ECNs and may be a strategy to increase filament stability and facilitate electron transport between repeating cytochrome subunits. Another factor contributing to AvECN thermal stability could be N-linked glycosylation, which is even more abundant than in PcECN (Figure S4).

Conserved heme stacking path in ECNs

It has been shown that there are preferred heme-heme pairing motifs used in proteins capable of efficient electron transfer.[16,17] Specifically, two major clusters were observed for the rotation angles and minimum edge-to-edge distances between porphyrin rings from two heme molecules: (1) ~3–5 Å distance and ~170°–180° rotation, corresponding to the antiparallel heme pair, and (2) ~4–6 Å distance and ~110°–150° rotation, corresponding to the "T-shape" heme pair (Figure 3A). The anti-

parallel heme pairs were often called "stacked" hemes in the past.[20,30] Here, we refer to them as antiparallel heme pairs to describe their packing nature more accurately. For instance, heme pairs in the well-studied *Shewanella* small tetra-heme cytochrome[31] and flavocytochrome c3[32] all fall into the preferred clusters. All possible porphyrin pairs in AvECN and PcECN fall into those two clusters, and in addition, the two types of heme stackings always occur alternately, that is, antiparallel → T-shape → antiparallel → T-shape... This observation also applies to *G. sulfurreducens* OmcS and OmcE filaments but is not entirely true in the OmcZ filament, as it has solvent-accessible heme molecules that break this stacking pattern (Figure 3A).

We then asked whether ECNs have evolved an optimized heme stacking path along the filament for long-range electron transfer, despite having no protein fold similarity. We compared all possible four-heme arrays, with the first two hemes being an antiparallel pair, in AvECN, PcECN, OmcS, OmcE, and OmcZ. To mainly focus on the heme location and ignore differences introduced by heme in-plane rotation, only five atoms per heme molecule, the iron and four N- atoms surrounding it, were used for this analysis. Strikingly, all such arrays, except those in OmcZ, are remarkably similar, with an RMSD (root-mean-square deviation) smaller than 1.1 Å (Figure 3B). This small RMSD is almost at the level of experimental error in the determination of the atomic coordinates being used in the comparisons. These results suggest that when an ECN wraps a solvent-inaccessible electron transport path, there is an optimized mode of heme stacking, with alternating antiparallel and T-shaped arrangements. In contrast,
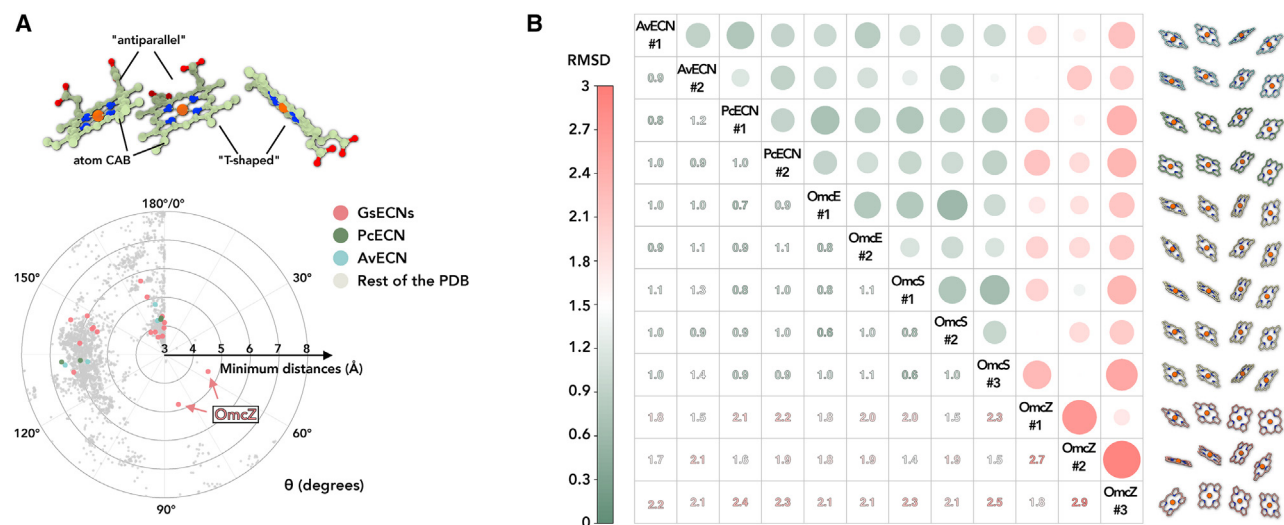
Figure 3. Conserved heme stacking in ECNs

(A) The heme-heme orientation plot. One heme can be aligned to the adjacent heme by a rotation and a translation. Only 25 non-hydrogen atoms in the porphyrin ring are used in the alignment. The heme (ID: HEC or HEM) pairs in all PDB structures were analyzed. Example of "antiparallel" and "T-shaped" pairs are shown. The minimum distances refer to the smallest distance between two porphyrin rings, regardless of the atom type. The angle θ was determined from the alignment rotation matrix between heme pairs. For example, θ = 0° means two porphyrin rings are perfectly parallel, while θ = 180° means two porphyrin rings are perfectly antiparallel (flipped). All porphyrin ring pairs with a minimum distance less than or equal to 8 Å are shown. The porphyrin ring pairs in *Geobacter*, *Pyrobaculum*, and *Archaeoglobus* ECNs are shown in red, green, and cyan, respectively.

(B) All-against-all comparison of all four-heme arrays in structures of ECNs. All possible four-heme arrays with the heme arrangements of "antiparallel" → "T-shaped" → "antiparallel" were extracted from structures of ECNs for this comparison. Tetra-heme ECNs, such as PcECN, AvECN, and OmcE, possess two of such four-heme arrays along the filament structure. On the other hand, hexa-heme ECN OmcS has three different arrays. The octa-heme ECN OmcZ, the only leaky ECN structure, also has three arrays owing to a solvent-accessible heme adopting a quite different pose breaking the conserved heme arrangements. The matrix is based on the pairwise RMSD comparison of 20 atoms between two arrays (five atoms per heme, including the iron and four surrounding nitrogen atoms). The resulting RMSD is shown in color, as indicated in the left bar. Extreme RMSD values are highlighted by larger dot sizes to emphasize very similar and different heme arrangements.

for an ECN that includes solvent-accessible hemes, OmcZ, a different pattern of hemes is present.

Evolution has optimized the four-heme array present in various protein families

Heme stacking patterns have been suggested to be similar in diverse protein families.[33] Because the four-heme arrays are conserved among fully insulated ECNs (those with a solvent-exposed heme only at filament ends) and because those ECNs transfer electrons on a micron scale, we wondered whether this type of four-heme array can be found in other protein families that transfer electrons over shorter distances. Therefore, we analyzed all multi-heme (both heme and heme c) entries in the PDB, identified all four-heme arrays similar to those seen in ECNs, and searched for the four-heme array in each PDB entry with the smallest RMSD compared with the input template (AvECN). To our surprise, among all the identified four-heme arrays, OmcZ has the largest RMSD of 1.7 Å, and all other four-heme arrays have an RMSD between 0.6 and 1.1 Å compared with AvECN. The results are similar if different four-heme arrays found in ECNs (such as OmcE or OmcS) are used as the reference. All those cytochromes detected were then analyzed by the DALI server,[24] and only one example in each protein fold is displayed in Figure 4. Despite no recognizable fold similarity and functional divergence, including fully insulated ECNs, a

leaky ECN (OmcZ), nitrite reductase, sulfite reductase, NrfB, photosynthetic cytochrome c552, hydroxylamine oxidoreductase, Mtr complex, and three types of oxidoreductases, this four-heme array pattern is ubiquitous in nature, suggesting that this is an evolutionarily optimized heme orientation for efficient electron transfer.

ECN homologs are widespread in archaea

We next examined the genomic loci containing the ECN-encoding genes in *P. calidifontis* and *A. veneficus*. This analysis was particularly revealing for *P. calidifontis*, in which the ECN gene is interspersed between apparent operons for respiratory nitrate reductase and cytochrome c biogenesis system, Ccm (Figure 5A). The nitrate reductase is a multicomponent integral membrane protein complex responsible for reduction of nitrite to ammonia, an energy-generating process supporting the growth of many hyperthermophiles, including *Pyrobaculum*, in extreme volcanic or geothermally active environments, such as terrestrial hot springs and deep-sea hydrothermal vents.[34,35] In contrast, the Ccm system is responsible for translocation of heme across the membrane and its covalent ligation to an apo-cytochrome c.[36] Thus, based on its genomic neighborhood, it is likely that PcECN participates in nitrate reduction and that its maturation depends on the Ccm machinery. Indeed, *P. calidifontis* has been shown to use nitrate as a final electron acceptor.[20]
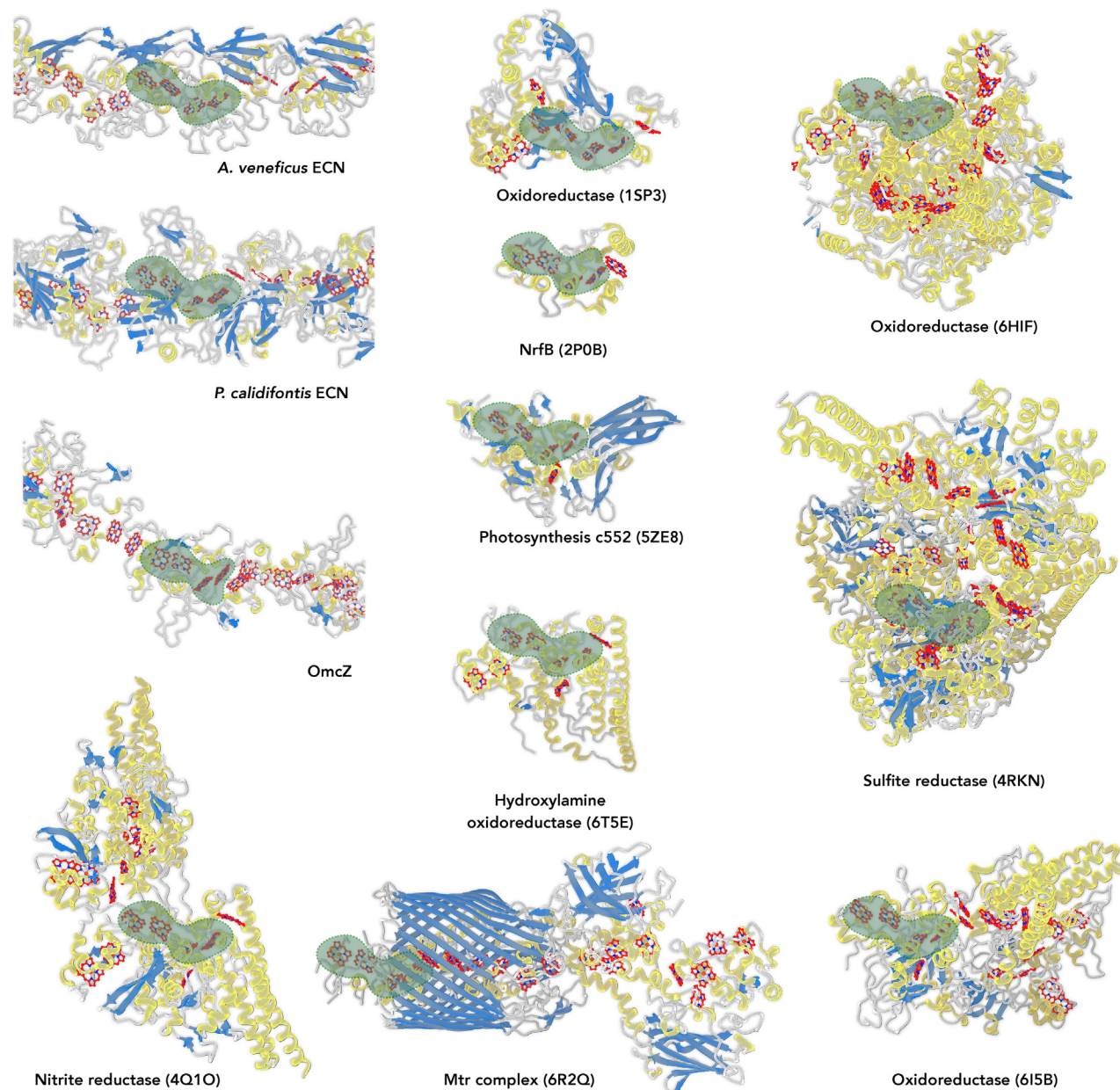
**Figure 4. Similar four-heme array present in various protein families**
Protein structures are colored by their secondary structures: α helices in yellow, β strands in blue, loops in gray. Heme molecules (heme and heme c) are colored in red. The identified four-heme arrays with minimum RMSD within the structure are enveloped in green.

Notably, PcECN has a predicted C-terminal transmembrane domain (residues 361–380), which was not present in our cryo-EM map, suggesting that it has been proteolytically processed prior to ECN assembly. The protein region upstream of the transmembrane domain does not carry canonical archaeosortase or exosortase recognition motifs.[38] However, immediately upstream of the PcECN gene, there is a gene encoding a putative serine protease, which is predicted to have an N-terminal Sec signal sequence and a C-terminal membrane anchor domain (Figure 5A), suggesting that the catalytic protease domain is located on the outside of the cell. Thus, it is likely that the C-terminal transmembrane domain of PcECN is processed by the adjacently encoded serine protease, following the incorporation of the heme molecule and maturation of the PcECN subunit.

Compared with PcECN, the genomic environment of the AvECN gene was less informative (Figure 5A). The gene is followed by a second copy of the AvECN-like gene (Arcve_0080; the corresponding proteins are 52% identical) and a gene encoding another multi-heme protein (Arcve_0079). However, the three-gene cassette is embedded among genes without apparent
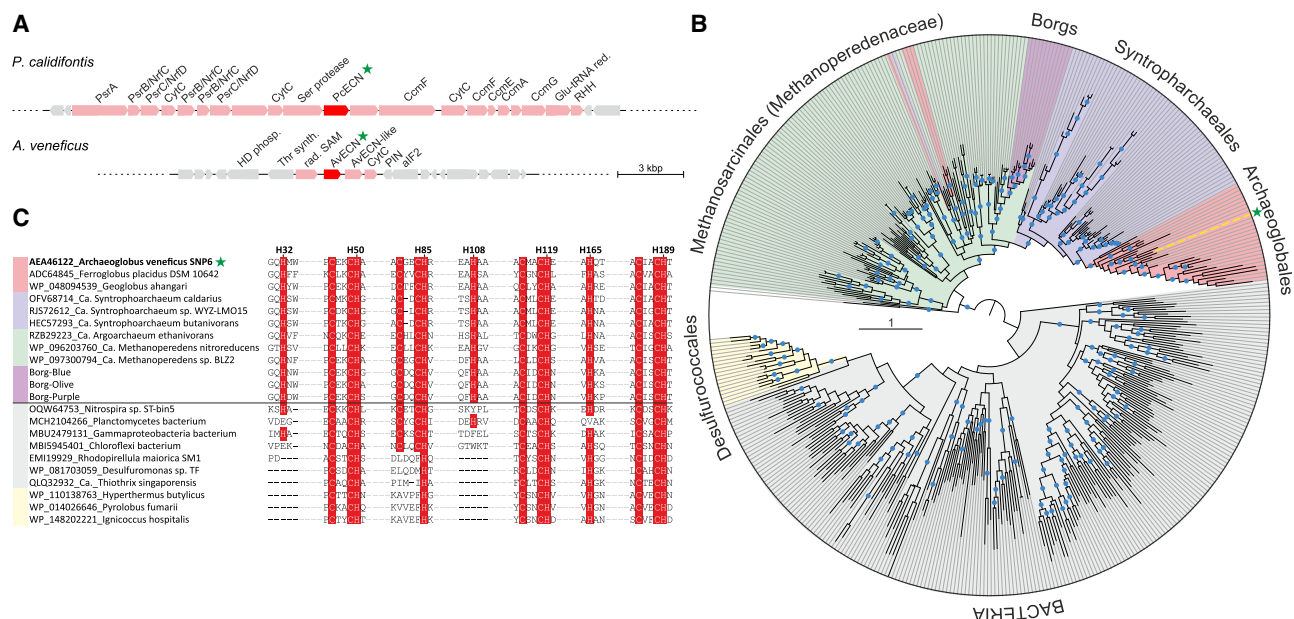
Figure 5. Diversity and distribution of archaeal ECN homologs

(A) ECN-encoding genomic loci in *P. calidifontis* and *A. veneficus*. ECN genes and functionally related genes are shown as red and pink arrows, respectively, whereas unrelated genes are shown in gray. Abbreviations: PrsA, Fe-S, 4Fe-4S cofactor-containing component of the polysulfide/nitrite reductase; PsrB/NrfC, 4Fe-4S cofactor-containing component of the polysulfide/nitrite reductase; PsrC/NrfD, polysulfide/nitrite reductase membrane component; CytC, cytochrome *c* family protein; CcmAEFG, cytochrome *c* biogenesis system components A, E, F, and G; RHH, ribbon-helix-helix DNA-binding protein; Glu-tRNA red, glutamyl-tRNA reductase; HD phosph, HD-superfamily phosphohydrolase; Thr synth, threonine synthase; rad. SAM, radical SAM superfamily enzyme; PIN, PIN-domain nuclease; aIF2, archaeal translation initiation factor 2.

(B) Mid-point rooted maximum likelihood phylogeny of AvECN homologs. Tree branches are colored according to the organism taxonomy, with the taxon names indicated next to the corresponding clades. Note the horizontal transfers from Methanosarcinales to Archaeoglobales and Syntrophoarchaeales are shown as pink and magenta inserts, respectively, within the green clade. The position of AvECN is indicated by yellow line and green star. Blue circles denote approximate likelihood ratio test (aLRT) branch supports higher than 90%. The scale bar represents the number of substitutions per site.

(C) Sequence motifs conserved in AvECN homologs. Archaeal groups are represented by 3 sequences each, whereas bacterial homologs are represented by 7 sequences. The name of each sequence includes GenBank accession number followed by a species name. In the case of Borgs, the sequences were downloaded from the supplemental information of Al-Shayeb et al.[37] Conserved His and Cys residues are highlighted on red background. The numbered His residues shown above the alignment correspond to the AvECN sequence. The horizontal line separates sequences belonging to the two major clades identified in the phylogeny shown in (B).

involvement in energy-generating processes or cytochrome maturation (e.g., threonine synthase or translation initiation factor 2).

To explore the phyletic distribution of the two archaeal ECN homologs, we performed PSI-BLAST searches queried with the corresponding sequences against the non-redundant GenBank protein sequence database. Whereas the homologs of PcECN were not detected outside the archaeal order Desulfurococcales (genera *Pyrobaculum* and *Pyrodictium*), AvECN were distributed more broadly (Figure 5B). In particular, AvECN homologs are widespread not only among other hyperthermophilic members of order Archaeoglobales but also among alkane-degrading archaea of the order Syntrophoarchaeales and methane oxidizers of the family Methanoperedenaceae (also known as ANME-2d; order Methanosarcinales).[39] Furthermore, AvECN homologs are conserved in multiple Borgs, a group of recently discovered extremely large (up to 1 Mbp) linear megaplasmids associated with methane-oxidizing Methanoperedens archaea.[37] Each Borg element contained two tandemly encoded ECN copies, similar to *A. veneficus* (Figure 5A). Notably, it has been suggested that Borgs provide Methanoper-

edens archaea access to genes that encode proteins involved in redox reactions and energy conservation and thereby assist in modulating greenhouse gas emissions.[37] We hypothesize that AvECN homologs play an important role in these processes by mediating long-range electron transfers. More distant homologs of AvECN are also present in diverse bacteria and hyperthermophilic archaea of the order Desulfurococcales (Figure 5B). In maximum likelihood phylogenetic analysis, AvECN homologs split into two major clades, with one clade including the archaeal proteins from the Archaeoglobales, Syntrophoarchaeales, and Methanoperedenaceae, including Borgs, and the other clade comprising bacterial and Desulfurococcales homologs. Notably, the branching pattern of the tree suggests that Archaeoglobales ECNs, including AvECN, have evolved from the Syntrophoarchaeales, which in turn have emerged from Methanoperedenaceae. Similarly, ECN homologs of Borgs have evidently been acquired from the Methanoperedenaceae host on a single occasion, followed by duplication and diversification within Borgs. Several more recent horizontal gene transfer events from Methanoperedenaceae to Archaeoglobales and

Syntrophoarchaeales were also detected (Figure 5B; DataS1). In the second clade, Desulfurococcales subclade emerges from within the diverse bacterial homologs, suggesting a bacteria-to-archaea horizontal gene transfer.

To analyze whether AvECN homologs in other archaea and bacteria are likely to form ECNs, we assessed the conservation of the amino acid motifs involved in heme attachment and coordination (Figure 5C). Whereas in Archaeoglobales, Syntrophoarchaeales, and Methanoperedenaceae, as well as Borgs, all motifs were well conserved, in bacterial and Desulfurococcales homologs, the motifs containing AvECN heme-coordinating H32 and H108 were largely missing, suggesting functional divergence. The conservation of the heme-coordinating motifs in AvECN homologs of Methanoperedens, Syntrophoarchaeales, and Borgs strongly suggests that these ecologically important archaea will produce structurally similar ECNs.

Evolutionary link between AvECN-like proteins and c552-family cytochromes

Although structure-based searches queried with ECN subunits failed to identity structural homologs, sensitive profile-profile searches queried with AvECN yielded a significant, albeit partial, hit to a c552-family protein from a purple sulfur photosynthetic bacterium *Thermochromatium tepidum*.[40] Similarly, when the AvECN homolog from a Planctomycetes bacterium was used as a query, c552 from *T. tepidum* was again identified as the best hit (HHsearch probability of 100%; Figures S5A and S5B). To further explore this potential relationship, we manually compared the structures of AvECN and c552 cytochrome (PDB: 5ZE8). When AvECN was aligned to c552 by four shared heme molecules, a set of α helices in AvECN overlapped quite well with part of the N-terminal domain (Pfam-13435) of c552 (Figures S5C–S5E), further supporting an evolutionary relationship between AvECN and c552 and suggesting that the two protein families have shared a common ancestor.

DISCUSSION

Starting from a bioinformatics approach aimed at finding potential extracellular cytochrome filaments in archaea, we identified three culturable organisms that appeared to be good candidates for having such filaments. We identified ECNs in two of these archaeal organisms, *P. calidifontis* and *A. veneficus*, and determined their atomic structures. Does this mean that ECNs are never produced by the third organism, *M. tindarius*? We think not, as it is quite possible that such filaments might be expressed by *M. tindarius* under different cultivation conditions. On the other hand, is it possible that *P. calidifontis* and *A. veneficus* are the only two archaeal species expressing such extracellular cytochrome filaments? This seems highly unlikely, and our results strongly suggest that such ECNs are ubiquitous in both bacteria and archaea that rely on long-range electron transfer for metabolism. This is consistent with the identification of numerous archaeal AvECN homologs in Archaeoglobales, Syntrophoarchaeales, and Methanoperedenaceae. Our results also establish that the extracellular cytochrome filaments that have been found in *G. sulfurreducens* are not unique.

Unlike *G. sulfurreducens* cytochrome filaments that lack substantial amounts of secondary structure and contain ~80% loops, PcECN and AvECN have significantly higher percentages of secondary structures at 33% and 44%, respectively. Generally, a low percentage of secondary structure is a common feature seen in electron-transporting multi-heme cytochromes,[41] mainly owing to the pressure of evolutionary selection focused on closely stacked heme arrangements for efficient electron transfer, rather than on a conserved protein fold. Interestingly, despite a relatively higher percentage of secondary structure, a similar protein fold for either PcECN or AvECN cannot be identified among known protein structures using conventional methods, such as DALI, suggesting that ECN structures are still very sparsely sampled. Nevertheless, sensitive profile-profile HMM comparisons pointed toward an evolutionary relationship between AvECN and c552-family proteins, suggesting that at least some ECNs have evolved from non-filamentous multi-heme cytochrome proteins.

Despite no fold similarity among the five structurally characterized ECNs, the heme path in insulated nanowires, which includes all existing structures of ECNs except for OmcZ, share a strikingly similar pattern, with alternating antiparallel and T-shaped arrangements. Although we have not been able to directly measure the conductivity of the PcECN and AvECN (see Limitations of the study), given the quaternary structure of the ECNs and the highly conserved heme packing, it is very likely that the two archaeal ECNs function in long-distance electron transfer with a similar conductivity as the OmcS and OmcE filaments. We also think that the existence of these filaments must be due to a strong selection given the biosynthetic cost, and the extracellular bacterial flagellar filament provides a good example. In stirred liquid culture, where motility conveys no advantage, bacterial cells lose the flagellar filament within only 10 days as a result of mutations in any of the large number of flagellar genes.[42] The conclusion was that mutants that fail to synthesize flagellin have a growth rate advantage of ~2% owing to the high biosynthetic cost of producing flagellin when it is not needed. Similarly, we would expect that there would be a large metabolic penalty for producing extracellular cytochrome polymers that can be microns long in the absence of an important role played by these polymers in long-range electron transport.

When looking at four-heme arrays, the RMSD among all insulated ECNs is less than 1.1 Å. Similar four-heme arrays can also be identified in multi-heme enzymes, implying that this arrangement is an optimal path for efficient electron transfer. This leads to another question: do the hemes always pack in antiparallel and T-shape alternatively in insulated ECNs? Conceivably, from a protein folding perspective, having more than two antiparallel c-type hemes could be rather challenging because each heme needs to be coordinated by two histidines and two thioether linkages from two cysteines. However, nothing seems to prevent a multi-heme cytochrome from having continuous T-shape packing of hemes, and it has recently been suggested that the electron transfer rate between T-shape hemes is similar to or less than an order of magnitude faster than that between antiparallel ones.[43–45] The current absence of evidence is not evidence of absence, and more structures of insulated ECNs are needed to address whether cytochrome nanowires containing a continuous T-shape packing of hemes exist.

In *Geobacter*, the expression of ECNs (OmcS, OmcE, and OmcZ) is tightly linked to a type IV pilus made of two chains, PilA-N and PilA-C. The pilin was proposed to form a periplasmic endopilus,[11] formerly called a pseudopilus, possibly functioning as a pump to aid the export of cytochrome filaments through a Type 2 Secretion System (T2SS).[18] However, it is unclear in archaea how ECNs are assembled and secreted to the extracellular space. Interestingly, the presence of the N-terminal signal sequences and signal peptidase cleavage sites suggests that pre-ECN subunits are externalized through the Sec pathway to the cell exterior. In the case of PcECN, the proximity of the gene to the cytochrome *c* biogenesis and maturation system, Ccm, further suggests that following the externalization, the pre-ECN subunits undergo maturation and heme loading by the Ccm machinery. These observations provide testable hypotheses for future research. The genetic neighborhood analysis suggests that PcECN is involved respiratory nitrate reduction, consistent with the evidence that *P. calidifontis* can use nitrate as a final electron acceptor.[20] The terminal acceptors of long-range electron transfer through AvECNs remain unclear. However, in the case of Methanoperedenaceae, it has been shown that for methane oxidation, these archaea can transfer electrons extracellularly to a number of soluble and insoluble electron acceptors, including sulfate, nitrate, and metal oxides.[46] The conservation and broad distribution of AvECN homologs in Methanoperedens, Syntrophoarchaeales, and Borgs suggest that long-range electron transfer associated with methane oxidation occurs through structurally similar ECNs, contributing to the modulation of greenhouse gas emissions.

Recent advances in cryo-EM have made it possible to directly and routinely determine a protein filament's atomic structure, allowing unambiguous protein identification.[11] It is thus not surprising that the application of these methods to both bacteria and archaea continue to show the existence of previously uncharacterized, functionally diverse extracellular filaments at an increasing rate.[21,47] We therefore expect that further studies of bacteria and archaea will reveal the existence and structure of many more ECNs. Given the enormous potential for such nanowires in applications such as biomedical devices, nanoelectronics, and bioenergy, we expect that further basic research in this area will be fruitful.

Limitations of the study

One of the limitations of this study is the lack of conductivity measurements for the archaeal extracellular cytochrome filaments. However, there are enormous experimental challenges in this regard. Most conductivity measurements are performed on air-dried samples.[48–50] The implicit assumption must be that the atomic structure of these filaments is unchanged from solution. However, we know from more than 80 years of structural biology that this cannot be the case,[51] and protein structure is only maintained in a fully hydrated state, which is either in solution or in a crystal in solution. There are two "competing" models for conductivity in extracellular filaments. One is that it arises from the stacking of aromatic residues in type IV pili, and the other is that it is due to stacked hemes. In both, a particular atomic structure needs to be precisely maintained to support such conductivity. Thus, air drying of type IV pili or cyto-

chrome filaments would unavoidably lead to the loss of atomic basis for conductivity. Consequently, there is little physiological relevance to the conductivity measured from denatured air-dried filaments.

There are additional limitations with existing techniques for measuring conductivity. For all insulated ECNs, hemes are only exposed at two ends of the filaments. Therefore, for a meaningful measurement, the electrodes would need to be perfectly aligned to physically touch exposed hemes at both ends of a filament, which is nearly impossible. Recently, OmcZ filaments have been stated to be 1,000×-fold more conductive than OmcS[48] despite their similar heme-heme packing. We hypothesized that the branched hemes in OmcZ, with a solvent-exposed heme in each subunit, accounted for the higher-measured conductivity.[17] Another problem in such conductivity measurements is that one does not really know what filaments are being measured. For example, *Pyrobaculum* produces at least three other extracellular filaments in addition to the cytochrome polymer. The atomic structures of two of them are already known,[21,52] and those filaments would be indistinguishable from cytochrome filaments under AFM (Atomic Force Microscopy), a technique used for the conductivity measurements. It is also apparent that DNA can be found in extracellular preparations of cytochrome filaments.[16,18] Interestingly, extracellular DNA has previously been reported to be conductive;[53] therefore, even the most careful attempts to measure conductivity of extracellular filaments may be thwarted by the DNA contamination.

In summary, current technology does not exist for reliably measuring the conductivity of individual fully hydrated filaments of known composition. We believe that the development of such technology will be important.

STAR★METHODS

Detailed methods are provided in the online version of this paper and include the following:

- KEY RESOURCES TABLE
- RESOURCE AVAILABILITY
  - Lead contact
  - Materials availability
  - Data and code availability
- EXPERIMENTAL MODEL AND STUDY PARTICIPANT DETAILS
  - Organism/Strain: *P. calidifontis* growth condition
  - Organism/Strain: *A. veneficus* growth condition
  - Organism/Strain: *M. tindarius* growth condition
- METHOD DETAILS
  - *P. calidifontis* filament preparation
  - *A. veneficus* filament preparation
  - *M. tindarius* filament preparation
  - Cryo-EM conditions and image processing
  - Model building of *P. calidifontis* and *A. veneficus* ECNs
  - Structural analysis of heme molecules in heme containing PDBs
  - Homology searches and phylogenetic analysis

SUPPLEMENTAL INFORMATION

Supplemental information can be found online at https://doi.org/10.1016/j.cell.2023.05.012.

AUTHOR CONTRIBUTIONS

F.W. initiated and developed the project. D.P.B. and V.C.-K. performed sample preparation. F.W. performed microscopy and image analysis. S.S.H., M.K., and F.W. did the bioinformatic analysis. J.L.F., M.K., and F.W. did the visualization. F.W., E.H.E., and M.K obtained funding, analyzed data, and supervised the research. D.P.B., V.C.-K., X.L., C.R., E.H.E., M.K., and F.W. wrote the manuscript with input from all authors.

DECLARATION OF INTERESTS

The authors declare no competing interests.

REFERENCES

1. Reguera, G. (2018). Microbial nanowires and electroactive biofilms. FEMS Microbiol. Ecol. *94*. https://doi.org/10.1093/femsec/fiy086.

2. Light, S.H., Su, L., Rivera-Lugo, R., Cornejo, J.A., Louie, A., Iavarone, A.T., Ajo-Franklin, C.M., and Portnoy, D.A. (2018). A flavin-based extracellular electron transfer mechanism in diverse Gram-positive bacteria. Nature *562*, 140–144. https://doi.org/10.1038/s41586-018-0498-z.

3. Shi, L., Dong, H., Reguera, G., Beyenal, H., Lu, A., Liu, J., Yu, H.Q., and Fredrickson, J.K. (2016). Extracellular electron transfer mechanisms between microorganisms and minerals. Nat. Rev. Microbiol. *14*, 651–662. https://doi.org/10.1038/nrmicro.2016.93.

4. Vargas, M., Kashefi, K., Blunt-Harris, E.L., and Lovley, D.R. (1998). Microbiological evidence for Fe(III) reduction on early Earth. Nature *395*, 65–67. https://doi.org/10.1038/25720.

5. Lovley, D.R. (2017). Syntrophy goes electric: direct interspecies electron transfer. Annu. Rev. Microbiol. *71*, 643–664. https://doi.org/10.1146/annurev-micro-030117-020420.

6. Wang, W., and Lee, D.J. (2021). Direct interspecies electron transfer mechanism in enhanced methanogenesis: a mini-review. Bioresour. Technol. *330*, 124980. https://doi.org/10.1016/j.biortech.2021.124980.

7. McGlynn, S.E., Chadwick, G.L., Kempes, C.P., and Orphan, V.J. (2015). Single cell activity reveals direct electron transfer in methanotrophic consortia. Nature *526*, 531–535. https://doi.org/10.1038/nature15512.

8. Wegener, G., Krukenberg, V., Riedel, D., Tegetmeyer, H.E., and Boetius, A. (2015). Intercellular wiring enables electron transfer between methanotrophic archaea and bacteria. Nature *526*, 587–590. https://doi.org/10.1038/nature15733.

9. Ha, P.T., Lindemann, S.R., Shi, L., Dohnalkova, A.C., Fredrickson, J.K., Madigan, M.T., and Beyenal, H. (2017). Syntrophic anaerobic photosynthesis via direct interspecies electron transfer. Nat. Commun. *8*, 13924. https://doi.org/10.1038/ncomms13924.

10. Liu, X., Huang, L., Rensing, C., Ye, J., Nealson, K.H., and Zhou, S. (2021). Syntrophic interspecies electron transfer drives carbon fixation and growth by Rhodopseudomonas palustris under dark, anoxic conditions. Sci. Adv. *7*. https://doi.org/10.1126/sciadv.abh1852.

11. Wang, F., Craig, L., Liu, X., Rensing, C., and Egelman, E.H. (2023). Microbial nanowires: type IV pili or cytochrome filaments? Trends Microbiol. *31*, 384–392.

12. Egelman, E.H. (2016). The current revolution in cryo-EM. Biophys. J. *110*, 1008–1012. https://doi.org/10.1016/j.bpj.2016.02.001.

13. Kühlbrandt, W. (2014). Cryo-EM enters a new era. eLife *3*, e03678. https://doi.org/10.7554/eLife.03678.

14. Wang, F., Gu, Y., O'Brien, J.P., Yi, S.M., Yalcin, S.E., Srikanth, V., Shen, C., Vu, D., Ing, N.L., Hochbaum, A.I., et al. (2019). Structure of microbial nanowires reveals stacked hemes that transport electrons over micrometers. Cell *177*, 361–369.e10. https://doi.org/10.1016/j.cell.2019.03.029.

15. Filman, D.J., Marino, S.F., Ward, J.E., Yang, L., Mester, Z., Bullitt, E., Lovley, D.R., and Strauss, M. (2019). Cryo-EM reveals the structural basis of long-range electron transport in a cytochrome-based bacterial nanowire. Commun. Biol. *2*, 219. https://doi.org/10.1038/s42003-019-0448-9.

16. Wang, F., Mustafa, K., Suciu, V., Joshi, K., Chan, C.H., Choi, S., Su, Z., Si, D., Hochbaum, A.I., Egelman, E.H., et al. (2022). Cryo-EM structure of an extracellular Geobacter OmcE cytochrome filament reveals tetrahaem packing. Nat. Microbiol. *7*, 1291–1300. https://doi.org/10.1038/s41564-022-01159-z.

17. Wang, F., Chan, C.H., Suciu, V., Mustafa, K., Ammend, M., Si, D., Hochbaum, A.I., Egelman, E.H., and Bond, D.R. (2022). Structure of Geobacter OmcZ filaments suggests extracellular cytochrome polymers evolved independently multiple times. eLife *11*. https://doi.org/10.7554/eLife.81551.

18. Gu, Y., Srikanth, V., Salazar-Morales, A.I., Jain, R., O'Brien, J.P., Yi, S.M., Soni, R.K., Samatey, F.A., Yalcin, S.E., and Malvankar, N.S. (2021). Structure of *Geobacter* pili reveals secretory rather than nanowire behaviour. Nature *597*, 430–434. https://doi.org/10.1038/s41586-021-03857-w.

19. Kletzin, A., Heimerl, T., Flechsler, J., van Niftrik, L., Rachel, R., and Klingl, A. (2015). Cytochromes c in archaea: distribution, maturation, cell architecture, and the special case of ignicoccus hospitalis. Front. Microbiol. *6*, 439. https://doi.org/10.3389/fmicb.2015.00439.

20. Amo, T., Paje, M.L., Inagaki, A., Ezaki, S., Atomi, H., and Imanaka, T. (2002). Pyrobaculum calidifontis sp. nov., a novel hyperthermophilic archaeon that grows in atmospheric air. Archaea *1*, 113–121. https://doi.org/10.1155/2002/616075.

21. Wang, F., Cvirkaite-Krupovic, V., Krupovic, M., and Egelman, E.H. (2022). Archaeal bundling pili of Pyrobaculum calidifontis reveal similarities between archaeal and bacterial biofilms. Proc. Natl. Acad. Sci. USA *119*, e2207037119. https://doi.org/10.1073/pnas.2207037119.

22. Jumper, J., Evans, R., Pritzel, A., Green, T., Figurnov, M., Ronneberger, O., Tunyasuvunakool, K., Bates, R., Žídek, A., Potapenko, A., et al. (2021). Highly accurate protein structure prediction with AlphaFold. Nature *596*, 583–589. https://doi.org/10.1038/s41586-021-03819-2.

23. Teufel, F., Almagro Armenteros, J.J., Johansen, A.R., Gíslason, M.H., Pihl, S.I., Tsirigos, K.D., Winther, O., Brunak, S., von Heijne, G., and Nielsen, H. (2022). SignalP 6.0 predicts all five types of signal peptides using protein language models. Nat. Biotechnol. *40*, 1023–1025. https://doi.org/10.1038/s41587-021-01156-3.

24. Holm, L. (2020). Using Dali for protein structure comparison. Methods Mol. Biol. *2112*, 29–42. https://doi.org/10.1007/978-1-0716-0270-6_3.

25. van Kempen, M., Kim, S.S., Tumescheit, C., Mirdita, M., Söding, J., and Steinegger, M. (2022). Foldseek: fast and accurate protein structure search https://doi.org/10.1101/2022.02.07.479398.

26. Wang, F., Baquero, D.P., Su, Z., Beltran, L.C., Prangishvili, D., Krupovic, M., and Egelman, E.H. (2020). The structures of two archaeal type IV pili illuminate evolutionary relationships. Nat. Commun. *11*, 3424. https://doi.org/10.1038/s41467-020-17268-4.

Cell
Article

CellPress

27. Wang, F., Cvirkaite-Krupovic, V., Kreutzberger, M.A.B., Su, Z., de Oliveira, G.A.P., Osinski, T., Sherman, N., DiMaio, F., Wall, J.S., Prangishvili, D., et al. (2019). An extensively glycosylated archaeal pilus survives extreme conditions. Nat. Microbiol. *4*, 1401–1410. https://doi.org/10.1038/s41564-019-0458-x.

28. Kreutzberger, M.A.B., Sonani, R.R., Liu, J., Chatterjee, S., Wang, F., Sebastian, A.L., Biswas, P., Ewing, C., Zheng, W., Poly, F., et al. (2022). Convergent evolution in the supercoiling of prokaryotic flagellar filaments. Cell *185*, 3487–3500.e14. https://doi.org/10.1016/j.cell.2022.08.009.

29. Huber, H., Jannasch, H., Rachel, R., Fuchs, T., and Stetter, K.O. (1997). Archaeoglobus veneficus sp. nov., a novel facultative chemolithoautotrophic hyperthermophilic sulfite reducer, isolated from abyssal black smokers. Syst. Appl. Microbiol. *20*, 374–380. https://doi.org/10.1016/S0723-2020(97)80005-7.

30. Mowat, C.G., and Chapman, S.K. (2005). Multi-heme cytochromes–new structures, new chemistry. Dalton Trans., 3381–3389. https://doi.org/10.1039/b505184c.

31. Leys, D., Meyer, T.E., Tsapin, A.S., Nealson, K.H., Cusanovich, M.A., and Van Beeumen, J.J. (2002). Crystal structures at atomic resolution reveal the novel concept of "electron-harvesting" as a role for the small tetra-heme cytochrome c. J. Biol. Chem. *277*, 35703–35711. https://doi.org/10.1074/jbc.M203866200.

32. Mowat, C.G., Moysey, R., Miles, C.S., Leys, D., Doherty, M.K., Taylor, P., Walkinshaw, M.D., Reid, G.A., and Chapman, S.K. (2001). Kinetic and crystallographic analysis of the key active site acid/base arginine in a soluble fumarate reductase. Biochemistry *40*, 12292–12298. https://doi.org/10.1021/bi011360h.

33. Soares, R., Costa, N.L., Paquete, C.M., Andreini, C., and Louro, R.O. (2022). A new paradigm of multiheme cytochrome evolution by grafting and pruning protein modules. Mol. Biol. Evol. *39*. https://doi.org/10.1093/molbev/msac139.

34. Jormakka, M., Yokoyama, K., Yano, T., Tamakoshi, M., Akimoto, S., Shimamura, T., Curmi, P., and Iwata, S. (2008). Molecular mechanism of energy conservation in polysulfide respiration. Nat. Struct. Mol. Biol. *15*, 730–737. https://doi.org/10.1038/nsmb.1434.

35. Afshar, S., Johnson, E., de Vries, S., and Schröder, I. (2001). Properties of a thermostable nitrate reductase from the hyperthermophilic archaeon Pyrobaculum aerophilum. J. Bacteriol. *183*, 5491–5495. https://doi.org/10.1128/JB.183.19.5491-5495.2001.

36. Sanders, C., Turkarslan, S., Lee, D.W., and Daldal, F. (2010). Cytochrome c biogenesis: the Ccm system. Trends Microbiol. *18*, 266–274. https://doi.org/10.1016/j.tim.2010.03.006.

37. Al-Shayeb, B., Schoelmerich, M.C., West-Roberts, J., Valentin-Alvarado, L.E., Sachdeva, R., Mullen, S., Crits-Christoph, A., Wilkins, M.J., Williams, K.H., Doudna, J.A., et al. (2022). Borgs are giant genetic elements with potential to expand metabolic capacity. Nature *610*, 731–736. https://doi.org/10.1038/s41586-022-05256-1.

38. Haft, D.H., Payne, S.H., and Selengut, J.D. (2012). Archaeosortases and exosortases are widely distributed systems linking membrane transit with posttranslational modification. J. Bacteriol. *194*, 36–48. https://doi.org/10.1128/JB.06026-11.

39. Borrel, G., Adam, P.S., McKay, L.J., Chen, L.X., Sierra-García, I.N., Sieber, C.M.K., Letourneur, Q., Ghozlane, A., Andersen, G.L., Li, W.J., et al. (2019). Wide diversity of methane and short-chain alkane metabolisms in uncultured archaea. Nat. Microbiol. *4*, 603–613. https://doi.org/10.1038/s41564-019-0363-3.

40. Chen, J.H., Yu, L.J., Boussac, A., Wang-Otomo, Z.Y., Kuang, T., and Shen, J.R. (2019). Properties and structure of a low-potential, penta-heme cytochrome c552 from a thermophilic purple sulfur photosynthetic bacterium thermochromatium tepidum. Photosynth. Res. *139*, 281–293. https://doi.org/10.1007/s11120-018-0507-y.

41. Edwards, M.J., White, G.F., Butt, J.N., Richardson, D.J., and Clarke, T.A. (2020). The crystal structure of a biological insulated transmembrane molecular wire. Cell *181*, 665–673.e10. https://doi.org/10.1016/j.cell.2020.03.032.

42. Macnab, R.M. (1992). Genetics and biogenesis of bacterial flagella. Annu. Rev. Genet. *26*, 131–158. https://doi.org/10.1146/annurev.ge.26.120192.001023.

43. Jiang, X., van Wonderen, J.H., Butt, J.N., Edwards, M.J., Clarke, T.A., and Blumberger, J. (2020). Which multi-heme protein complex transfers electrons more efficiently? Comparing MtrCAB from Shewanella with OmcS from Geobacter. J. Phys. Chem. Lett. *11*, 9421–9425. https://doi.org/10.1021/acs.jpclett.0c02842.

44. van Wonderen, J.H., Hall, C.R., Jiang, X., Adamczyk, K., Carof, A., Heisler, I., Piper, S.E.H., Clarke, T.A., Watmough, N.J., Sazanovich, I.V., et al. (2019). Ultrafast light-driven electron transfer in a Ru(II)tris(bipyridine)-labeled multiheme cytochrome. J. Am. Chem. Soc. *141*, 15190–15200. https://doi.org/10.1021/jacs.9b06858.

45. van Wonderen, J.H., Adamczyk, K., Wu, X., Jiang, X., Piper, S.E.H., Hall, C.R., Edwards, M.J., Clarke, T.A., Zhang, H., Jeuken, L.J.C., et al. (2021). Nanosecond heme-to-heme electron transfer rates in a multiheme cytochrome nanowire reported by a spectrally unique His/Met-ligated heme. Proc. Natl. Acad. Sci. USA *118*. https://doi.org/10.1073/pnas.2107939118.

46. Scheller, S., Yu, H., Chadwick, G.L., McGlynn, S.E., and Orphan, V.J. (2016). Artificial electron acceptors decouple archaeal methane oxidation from sulfate reduction. Science *351*, 703–707. https://doi.org/10.1126/science.aad7154.

47. Böhning, J., Ghrayeb, M., Pedebos, C., Abbas, D.K., Khalid, S., Chai, L., and Bharat, T.A.M. (2022). Donor-strand exchange drives assembly of the TasA scaffold in Bacillus subtilis biofilms. Nat. Commun. *13*, 7082. https://doi.org/10.1038/s41467-022-34700-z.

48. Yalcin, S.E., O'Brien, J.P., Gu, Y., Reiss, K., Yi, S.M., Jain, R., Srikanth, V., Dahl, P.J., Huynh, W., Vu, D., et al. (2020). Electric field stimulates production of highly conductive microbial OmcZ nanowires. Nat. Chem. Biol. *16*, 1136–1142. https://doi.org/10.1038/s41589-020-0623-9.

49. Dahl, P.J., Yi, S.M., Gu, Y., Acharya, A., Shipps, C., Neu, J., O'Brien, J.P., Morzan, U.N., Chaudhuri, S., Guberman-Pfeffer, M.J., et al. (2022). A 300-fold conductivity increase in microbial cytochrome nanowires due to temperature-induced restructuring of hydrogen bonding networks. Sci. Adv. *8*, eabm7193. https://doi.org/10.1126/sciadv.abm7193.

50. Szmuc, E., Walker, D.J.F., Kireev, D., Akinwande, D., Lovley, D.R., Keitz, B., and Ellington, A. (2023). Engineering *Geobacter* pili to produce metal:-organic filaments. Biosens. Bioelectron. *222*, 114993. https://doi.org/10.1016/j.bios.2022.114993.

51. Bernal, J.D., Fankuchen, I., and Perutz, M. (1938). An x-ray study of chymotrypsin and haemoglobin. Nature *141*, 523–524.

52. Beltran, L.C., Cvirkaite-Krupovic, V., Miller, J., Wang, F., Kreutzberger, M.A.B., Patkowski, J.B., Costa, T.R.D., Schouten, S., Levental, I., Conticello, V.P., et al. (2023). Archaeal DNA-import apparatus is homologous to bacterial conjugation machinery. Nat. Commun. *14*, 666. https://doi.org/10.1038/s41467-023-36349-8.

53. Saunders, S.H., Tse, E.C.M., Yates, M.D., Otero, F.J., Trammell, S.A., Stemp, E.D.A., Barton, J.K., Tender, L.M., and Newman, D.K. (2020). Extracellular DNA promotes efficient extracellular electron transfer by pyocyanin in *Pseudomonas aeruginosa* biofilms. Cell *182*, 919–932.e19. https://doi.org/10.1016/j.cell.2020.07.006.

54. Trofimov, A.A., Polyakov, K.M., Lazarenko, V.A., Popov, A.N., Tikhonova, T.V., Tikhonov, A.V., and Popov, V.O. (2015). Structural study of the X-ray-induced enzymatic reaction of octahaem cytochrome C nitrite reductase. Acta Crystallogr. D Biol. Crystallogr. *71*, 1087–1094.

55. Mowat, C.G., Rothery, E., Miles, C.S., McIver, L., Doherty, M.K., Drewette, K., Taylor, P., Walkinshaw, M.D., Chapman, S.K., and Reid, G.A. (2004). Octaheme tetrathionate reductase is a respiratory enzyme with novel heme ligation. Nat. Struct. Mol. Biol. *11*, 1023–1024. https://doi.org/10.1038/nsmb827.

56. Clarke, T.A., Cole, J.A., Richardson, D.J., and Hemmings, A.M. (2007). The crystal structure of the pentahaem c-type cytochrome NrfB and characterization of its solution-state interaction with the pentahaem nitrite reductase NrfA. Biochem. J. *406*, 19–30. https://doi.org/10.1042/BJ20070321.

57. Akram, M., Dietl, A., Müller, M., and Barends, T.R.M. (2021). Purification of the key enzyme complexes of the anammox pathway from DEMON sludge. Biopolymers *112*, e23428. https://doi.org/10.1002/bip.23428.

58. Akram, M., Dietl, A., Mersdorf, U., Prinz, S., Maalcke, W., Keltjens, J., Ferousi, C., de Almeida, N.M., Reimann, J., Kartal, B., et al. (2019). A 192-heme electron transfer network in the hydrazine dehydrogenase complex. Sci. Adv. *5*, eaav4310. https://doi.org/10.1126/sciadv.aav4310.

59. Hermann, B., Kern, M., La Pietra, L., Simon, J., and Einsle, O. (2015). The octahaem MccA is a haem c-copper sulfite reductase. Nature *520*, 706–709. https://doi.org/10.1038/nature14109.

60. Costa, N.L., Hermann, B., Fourmond, V., Faustino, M.M., Teixeira, M., Einsle, O., Paquete, C.M., and Louro, R.O. (2019). How thermophilic Gram-positive organisms perform extracellular electron transfer: characterization of the cell surface terminal reductase OcwA. mBio *10*. https://doi.org/10.1128/mBio.01210-19.

61. König, H., and Stetter, K.O. (1982). Isolation and characterization of Methanolobus tindarius, sp. nov., a coccoid methanogen growing only on methanol and methylamines. Zentralblatt für Bakteriologie Mikrobiologie und Hygiene: I. Abt. Originale C: Allgemeine, angewandte und ökologische Mikrobiologie *3*, 478–490. https://doi.org/10.1016/S0721-9571(82)80005-7.

62. Punjani, A., Rubinstein, J.L., Fleet, D.J., and Brubaker, M.A. (2017). cryoSPARC: algorithms for rapid unsupervised cryo-EM structure determination. Nat. Methods *14*, 290–296. https://doi.org/10.1038/nmeth.4169.

63. Pettersen, E.F., Goddard, T.D., Huang, C.C., Meng, E.C., Couch, G.S., Croll, T.I., Morris, J.H., and Ferrin, T.E. (2021). UCSF ChimeraX: structure visualization for researchers, educators, and developers. Protein Sci. *30*, 70–82. https://doi.org/10.1002/pro.3943.

64. Afonine, P.V., Poon, B.K., Read, R.J., Sobolev, O.V., Terwilliger, T.C., Urzhumtsev, A., and Adams, P.D. (2018). Real-space refinement in PHENIX for cryo-EM and crystallography. Acta Crystallogr. D Struct. Biol. *74*, 531–544. https://doi.org/10.1107/S2059798318006551.

65. Emsley, P., and Cowtan, K. (2004). Coot: model-building tools for molecular graphics. Acta Crystallogr. D Biol. Crystallogr. *60*, 2126–2132. https://doi.org/10.1107/S0907444904019158.

66. Williams, C.J., Headd, J.J., Moriarty, N.W., Prisant, M.G., Videau, L.L., Deis, L.N., Verma, V., Keedy, D.A., Hintze, B.J., Chen, V.B., et al. (2018). MolProbity: more and better reference data for improved all-atom structure validation. Protein Sci. *27*, 293–315. https://doi.org/10.1002/pro.3330.

67. Pfab, J., Phan, N.M., and Si, D. (2021). DeepTracer for fast de novo cryo-EM protein structure modeling and special studies on CoV-related complexes. Proc. Natl. Acad. Sci. USA *118*. https://doi.org/10.1073/pnas.2017525118.

68. Chang, L., Wang, F., Connolly, K., Meng, H., Su, Z., Cvirkaite-Krupovic, V., Krupovic, M., Egelman, E.H., and Si, D. (2022). DeepTracer-ID: de novo protein identification from cryo-EM maps. Biophys. J. *121*, 2840–2848. https://doi.org/10.1016/j.bpj.2022.06.025.

69. Egelman, E.H. (2010). Reconstruction of helical filaments and tubes. Methods Enzymol. *482*, 167–183. https://doi.org/10.1016/S0076-6879(10)82006-3.

70. Rohou, A., and Grigorieff, N. (2015). CTFFIND4: fast and accurate defocus estimation from electron micrographs. J. Struct. Biol. *192*, 216–221. https://doi.org/10.1016/j.jsb.2015.08.008.

71. Zheng, S.Q., Palovcak, E., Armache, J.P., Verba, K.A., Cheng, Y., and Agard, D.A. (2017). MotionCor2: anisotropic correction of beam-induced motion for improved cryo-electron microscopy. Nat. Methods *14*, 331–332. https://doi.org/10.1038/nmeth.4193.

72. Egelman, E.H. (2000). A robust algorithm for the reconstruction of helical filaments using single-particle methods. Ultramicroscopy *85*, 225–234. https://doi.org/10.1016/S0304-3991(00)00062-0.

73. Afonine, P.V., Klaholz, B.P., Moriarty, N.W., Poon, B.K., Sobolev, O.V., Terwilliger, T.C., Adams, P.D., and Urzhumtsev, A. (2018). New tools for the analysis and validation of cryo-EM maps and atomic models. Acta Crystallogr. D Struct. Biol. *74*, 814–840. https://doi.org/10.1107/S2059798318009324.

74. Pettersen, E.F., Goddard, T.D., Huang, C.C., Couch, G.S., Greenblatt, D.M., Meng, E.C., and Ferrin, T.E. (2004). UCSF Chimera–a visualization system for exploratory research and analysis. J. Comput. Chem. *25*, 1605–1612. https://doi.org/10.1002/jcc.20084.

75. Rodrigues, M.L., Oliveira, T.F., Pereira, I.A., and Archer, M. (2006). X-ray structure of the membrane-bound cytochrome c quinol dehydrogenase NrfH reveals novel haem coordination. EMBO J. *25*, 5951–5960. https://doi.org/10.1038/sj.emboj.7601439.

76. Steinegger, M., and Söding, J. (2017). MMseqs2 enables sensitive protein sequence searching for the analysis of massive data sets. Nat. Biotechnol. *35*, 1026–1028. https://doi.org/10.1038/nbt.3988.

77. Capella-Gutiérrez, S., Silla-Martínez, J.M., and Gabaldón, T. (2009). trimAl: a tool for automated alignment trimming in large-scale phylogenetic analyses. Bioinformatics *25*, 1972–1973. https://doi.org/10.1093/bioinformatics/btp348.

78. Minh, B.Q., Schmidt, H.A., Chernomor, O., Schrempf, D., Woodhams, M.D., von Haeseler, A., and Lanfear, R. (2020). IQ-TREE 2: new models and efficient methods for phylogenetic inference in the genomic era. Mol. Biol. Evol. *37*, 1530–1534. https://doi.org/10.1093/molbev/msaa015.

79. Letunic, I., and Bork, P. (2021). Interactive tree of life (iTOL) v5: an online tool for phylogenetic tree display and annotation. Nucleic Acids Res. *49*, W293–W296. https://doi.org/10.1093/nar/gkab301.

80. Steinegger, M., Meier, M., Mirdita, M., Vöhringer, H., Haunsberger, S.J., and Söding, J. (2019). HH-suite3 for fast remote homology detection and deep protein annotation. BMC Bioinformatics *20*, 473. https://doi.org/10.1186/s12859-019-3019-7.

Cell
Article

CellPress

STAR★METHODS

KEY RESOURCES TABLE

REAGENT or RESOURCE	SOURCE	IDENTIFIER
Chemicals, peptides, and recombinant proteins		
Tryptone	Gibco	Cat #: 211705
Yeast extract	Gibco	Cat #: 212750
Phosphotungstic acid (PTA)	Electron Microscopy Sciences	Cat #: 19502-1
Uranyl acetate solution	Electron Microscopy Sciences	Cat #: 22400-2
Sodium thiosulfate	Sigma-Aldrich	Cat #: 217263
Sodium chloride	Sigma-Aldrich	Cat #: S9888
Potassium chloride	Sigma-Aldrich	Cat #: P9333
Magnesium chloride	Sigma-Aldrich	Cat #: M8266
Ammonium chloride	Sigma-Aldrich	Cat #: 326372
Calcium chloride	Sigma-Aldrich	Cat #: C4901
Potassium phosphate dibasic	Sigma-Aldrich	Cat #: P3786
Ammonium iron(II) sulfate hexahydrate	Sigma-Aldrich	Cat #: 203505
Resazurin sodium salt	Sigma-Aldrich	Cat #: R7017
Sodium bicarbonate	Sigma-Aldrich	Cat #: S6014
Sodium sulfite	Sigma-Aldrich	Cat #: S0505
Sodium acetate	Sigma-Aldrich	Cat #: S2886
Sodium sulfide	Sigma-Aldrich	Cat #: 431648
Deposited data		
G. sulfurreducens OmcS cryo-EM model	Wang et al.[14]	PDB 6EF8
G. sulfurreducens OmcE cryo-EM model	Wang et al.[16]	PDB 7TFS
G. sulfurreducens OmcZ cryo-EM model	Wang et al.[17]	PDB 8D9M
G. sulfurreducens type IV pilus cryo-EM model	Wang et al.[16]	PDB 7TGG
T. tepidum c552-family protein	Chen et al.[40]	PDB 5ZE8
T. nitratireducens nitrite reductase	Lazarenko et al.[54]	PDB 4Q1O
S. oneidensis oxidoreductase	Mowat et al.[55]	PDB 1SP3
E. coli NrfB	Clarke et al.[56]	PDB 2P0B
B. fulgida hydroxylamine oxidoreductase	Akram et al.[57]	PDB 6T5E
S. baltica Mtr complex	Edwards et al.[41]	PDB 6R2Q
K. stuttgartiensis hydrazine dehydrogenase	Akram et al.[58]	PDB 6HIF
W. succinogenes sulfite reductase	Hermann et al.[59]	PDB 4RKN
T. potens oxidoreductase	Costa et al.[60]	PDB 6I5B
P. calidifontis ECN, cryo-EM map	This paper	EMD-27911
P. calidifontis ECN, atomic model	This paper	PDB 8E5F
A. veneficus ECN, cryo-EM map	This paper	EMD-27912
A. veneficus ECN, atomic model	This paper	PDB 8E5G
Experimental models: Organisms/strains		
Pyrobaculum calidifontis	Amo et al.[20]	DSM 21063
Archaeoglobus veneficus	Huber et al.[29]	DSM 11195
Methanolobus tindarius	König et al.[61]	DSM 2278
Software and algorithms		
cryoSPARC	Punjani et al.[62]	https://cryosparc.com
ChimeraX	Pettersen et al.[63]	https://www.cgl.ucsf.edu/chimerax
Phenix	Afonine et al.[64]	https://phenix-online.org

(Continued on next page)

Continued

REAGENT or RESOURCE	SOURCE	IDENTIFIER
Coot	Emsley et al.[65]	https://www2.mrc-lmb.cam.ac.uk/personal/pemsley/coot
MolProbity	Williams et al.[66]	http://molprobity.biochem.duke.edu
AlphaFold2	Jumper et al.[22]	https://alphafold.ebi.ac.uk
DeepTracer	Pfab et al.[67]	https://deeptracer.uw.edu/
DeepTracer-ID	Chang et al.[68]	https://deeptracer.uw.edu/deeptracerid-new-job
Foldseek	van Kempen et al.[25]	https://search.foldseek.com/search
DALI	Holm et al.[24]	http://ekhidna2.biocenter.helsinki.fi/dali/
IHRSR-spider	Egelman[69]	https://joachimfranklab.org/research/software/

RESOURCE AVAILABILITY

Lead contact
Further information and requests for resources and reagents should be directed to and will be fulfilled by the lead contact, Fengbin Wang, jerrywang@uab.edu.

Materials availability
This study did not generate any new unique reagents.

Data and code availability
- Protein models built from cryo-EM maps have been deposited at Protein Data Bank and are publicly available as of the date of publication. The corresponding cryo-EM maps have been deposited at the Electron Microscopy Data Bank. The Entry IDs are listed in the key resources table. Microscopy raw data reported in this paper will be shared by the lead contact upon request.
- This paper didn't generate any original code.
- Any additional information required to reanalyze the data reported in this paper is available from the lead contact upon request.

EXPERIMENTAL MODEL AND STUDY PARTICIPANT DETAILS

Organism/Strain: *P. calidifontis* growth condition
Pyrobaculum calidifontis DSM 21063 cells were purchased from the DSMZ culture collection and grown in 1090 medium (0.1% yeast extract, 1.0% tryptone, 0.3% sodium thiosulfate, pH 7) at 90 °C without agitation. Preculture (30 mL) was started from a 200 μL cryo-stock, grown for 2 d and then diluted into 200 mL of fresh medium. When OD600 reached ~0.2, the cells were collected by centrifugation (Sorval SLA1500 rotor, 7,000 rpm, 10 min, 20 °C).

Organism/Strain: *A. veneficus* growth condition
Archaeoglobus veneficus DSM 11195 cells were purchased from the DSMZ culture collection. Three *A. veneficus* cultures (40 mL each) were grown at 75°C in 100 mL serum bottles under strict anaerobic conditions in DSMZ medium 796, as described previously.[29]

Organism/Strain: *M. tindarius* growth condition
Methanolobus tindarius DSM 2278 was purchased from the DSMZ culture collection. *M. tindarius* cells (40 mL) were grown at room temperature in a 100 mL serum bottle under strict anaerobic conditions in DSMZ medium 233, as described previously.[61]

METHOD DETAILS

P. calidifontis filament preparation
The resultant pellet was resuspended in 4 mL of phosphate-buffered saline (PBS) buffer, and the cell suspension was vortexed for 15 min to shear off the extracellular filaments. The cells were removed by centrifugation (Eppendorf F-35-6-30 rotor, 7,830 rpm, 20 min, 20 °C). The supernatant was collected and the filaments were pelleted by ultracentrifugation (Beckman SW60Ti rotor, 38,000 rpm, 2 h, 15 °C). After the run, the supernatant was removed, and the pellet was resuspended in 200 μL of PBS.

A. veneficus filament preparation
After three days of incubation, cultures were mixed and the majority of cells were removed by centrifugation (Eppendorf F-35-6-30 rotor, 7,830 rpm, 20 min, 20 °C). The supernatant was recovered, and filaments were collected and concentrated by

ultracentrifugation (158,728 × *g*, 3 h, 15 °C, Beckman 45 Ti rotor). After the run, the supernatant was carefully removed, and the pellet was resuspended in 300 µL of PBS.

M. tindarius filament preparation

After four days of incubation, cells were removed by centrifugation (Eppendorf F-35-6-30 rotor, 7,830 rpm, 20 min, 20 °C). The supernatant was recovered and filaments were collected and concentrated by ultracentrifugation (158,728 × *g*, 3 h, 15 °C, Beckman 45 Ti rotor). After the run, the supernatant was carefully removed, and the pellet was resuspended in 300 µL of PBS.

Cryo-EM conditions and image processing

The cell appendage sample (ca. 3.5-4.5 µl) was applied to glow-discharged lacey carbon grids and then plunge frozen using an EM GP Plunge Freezer (Leica). The cryo-EMs were collected on a 300 keV Titan Krios with a K3 camera (University of Virginia) at 1.08 Å/pixel and a total dose of ca. 50 e/Å^2. First, patch motion corrections and CTF estimations were done in cryoSPARC.[62,70,71] Next, particles were auto-picked by "Filament Tracer". All auto-picked particles were subsequently 2D classified with multiple rounds, and all particles in bad 2D averages were removed. After this, the *P. calidifontis* dataset had 101,864 particles left with a shift of 36 pixels between adjacent boxes, while the *A. veneficus* dataset had 92,602 particles left with the same 36-pixel shift. Next, the possible helical symmetries were calculated from an averaged power spectrum for each filament species generated from the raw particles. There is only one possibility for helical symmetry for both filaments, and the volume hand was determined by the hand of α-helices in the map.[69,72] After that, 3D reconstruction was performed using "Helical Refinement" first, and then using "Non-uniform Refinement". The resolution of each reconstruction was estimated by Map:Map FSC, Model:Map FSC, and d$_{99}$.[73] The final volumes were then sharpened with a negative B-factor automatically estimated in cryoSPARC, and the statistics are listed in Table S1.

Model building of *P. calidifontis* and *A. veneficus* ECNs

The density corresponding to a single *P. calidifontis* ECN subunit was segmented from the experimental cryo-EM density using Chimera.[74] Without using prior knowledge, placing heme molecules into the cryo-EM map at this resolution is challenging, especially while ligands are not included in AlphaFold predictions. Therefore, to better refine heme interacting areas at this resolution, bond/angle restraints for the heme molecule itself, His-Fe, and Cys-heme thioester bonds were restricted based on the geometries obtained in high-resolution crystal structures such as NrfB[56] (PDB 2P0B) and NrfHA[75] (PDB 2J7A). Similar refinement strategies have been used for *G. sulfurreducens* ECNs.[14,16,17] MolProbity[66] was used to evaluate the quality of the filament model. Similar to the model building of *P. calidifontis* cytochrome filaments, the single subunit map of *A. veneficus* was segmented. The subsequent 3D reconstructions and refinement are similar to the *P. calidifontis* case. The refinement statistics of both PcECN and AvECN are shown in Table S1.

### Structural analysis of heme molecules in heme containing PDBs

All structural coordinates with heme ligand (HEC or/and HEM) were downloaded from the Protein Data Bank. All possible heme pairs were then filtered with a minimum distance less than or equal to 8 Å between two porphyrin rings, using the "contact" command in UCSF-ChimeraX.[63] For each qualified pair, the rotation matrix between two hemes was generated in ChimeraX using the "align" command. The rotation angle θ was then calculated from the rotation matrix with the following equation, where tr is the trace of the rotation matrix. For the four-heme array analysis, the RMSD value between different four-heme arrays were also generated in ChimeraX using the "align" command.

$$|\theta| = \arccos\left(\frac{tr(R) - 1}{2}\right)$$

Homology searches and phylogenetic analysis

Homologs of PcECN and AvECN were collected by PSI-BLAST (5 iterations, inclusion E-value threshold of 1e-06) against non-redundant protein sequence database at NCBI. Due to large number of homologs, the highly similar bacterial sequences in the obtained dataset were then filtered to 50% identity over 80% of protein length using MMseq2.[76] All sequences shorter than 200 aa and longer than 400 aa were purged to discard partial sequences and to avoid potential problems with sequence alignment. This dataset was supplemented with ECN homologs from Borgs, which were identified using AvECN as a query in BLASTP searches (default parameters) against the Borg proteomes obtained.[37] Each of the following Borgs contained two AvECN homologs: Borg-Black, Borg-Blue, Borg-Brown, Borg-Olive, Borg-Orange and Borg-Purple. Multiple sequence alignment was built using MAFFT with the G-INS-1 option. The poorly conserved positions were removed using trimal with the gap threshold of 0.2.[77] Maximum likelihood phylogenetic analysis was performed using IQ-Tree v1.6.12[78] with the best amino acid substitution model selected for the alignment being WAG+I+G4. Brach support was assessed using the nonparametric SH-aLRT test. The phylogeny was visualized using iTOL v6.[79] Sensitive searches based on comparison of profile hidden Markov models (HMM) were performed using HHsearch from the HH-suite package v3.[80] Signal peptides and signal peptidase I cleavage sequences were predicted using SignalP v6.[23]

Supplemental figures

A

B

C

D
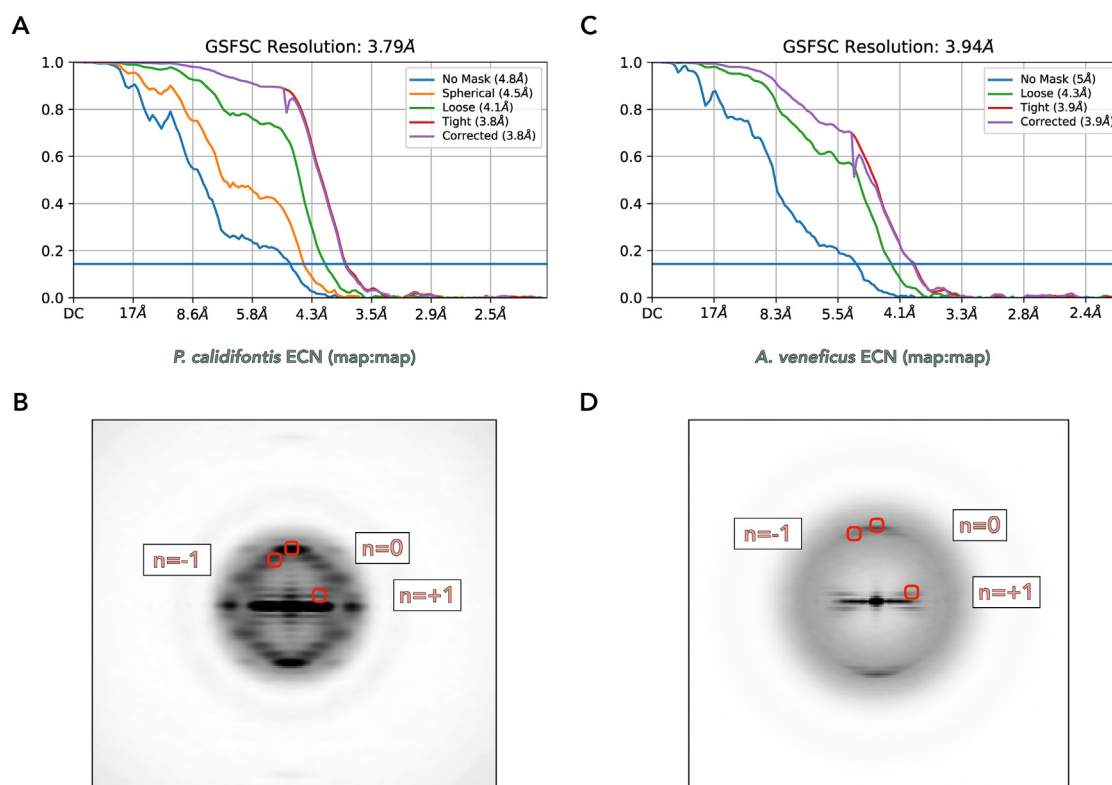
Figure S1. Fourier shell correlation (FSC) calculations and average power spectrum, related to Figures 1 and 2
(A) The map:map FSC calculation of *P. calidifontis* ECN (0.143 cutoff).
(B) The average power spectrum from PcECN raw particles aligned to the same axis.
(C) The map:map FSC calculation of *A. veneficus* ECN (0.143 cutoff).
(D) The average power spectrum from AvECN raw particles aligned to the same axis.
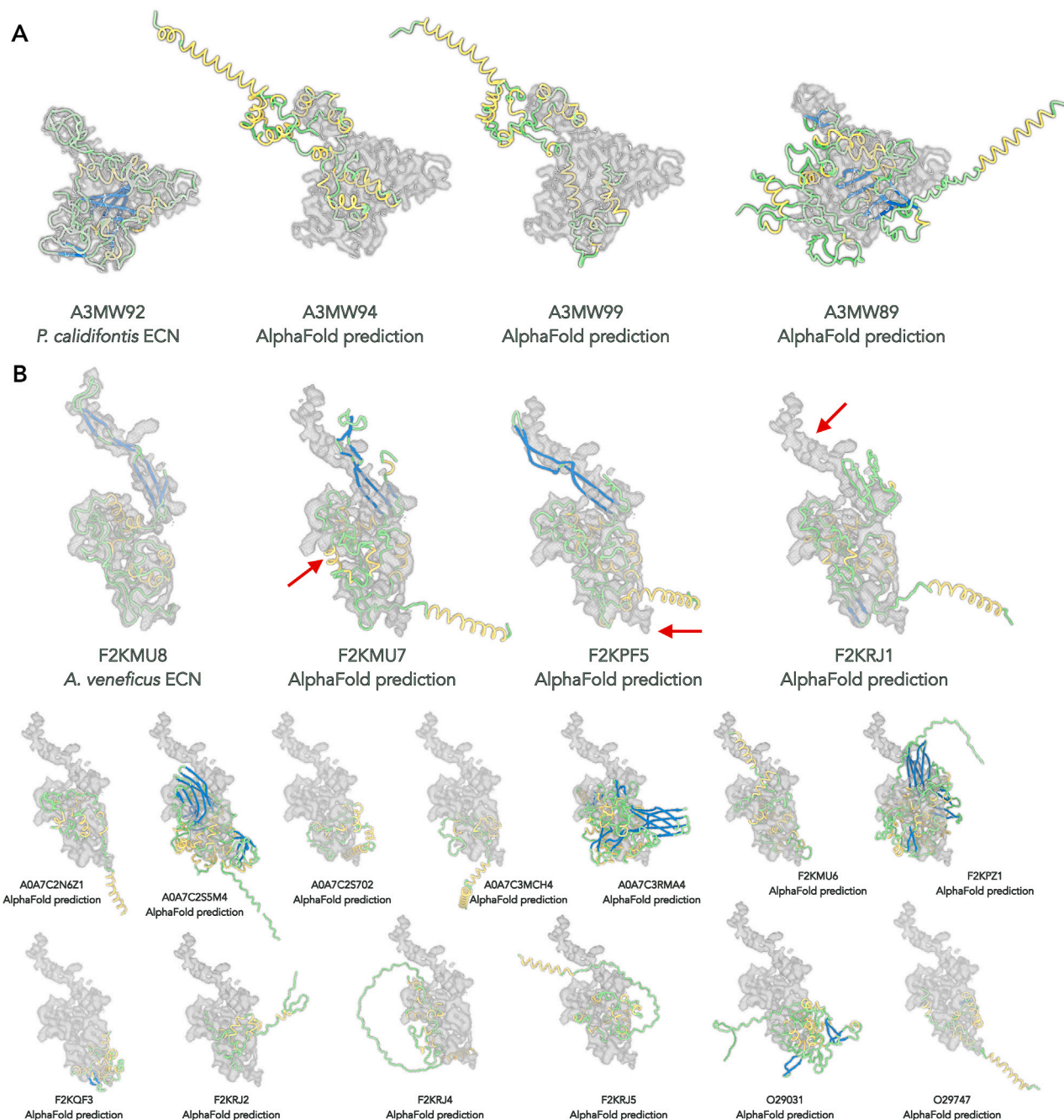
Figure S2. ECN protein identification from cryo-EM maps, related to Figures 1 and 2

(A) AlphaFold2 predictions of multi-heme cytochromes containing three or more CxxCH motifs in *P. calidifontis* were docked into the cryo-EM map corresponding to a single protein subunit. The color codes are as follows: α helices are yellow, β sheets are blue, and loops are green.

(B) AlphaFold2 predictions of multi-heme cytochromes containing three or more CxxCH motifs in *A. veneficus* were docked into the cryo-EM map corresponding to a single protein subunit. The color code is the same as in (A). The area of the AlphaFold2 predictions that cannot be possibly adjusted and fit into the map are highlighted by red arrows.

A

PcECN   MKKFPALITTLLLLAVFVAA TYGPPYSYNHPTNCISCHSNSTGTANSQALSGLTSGPAAGACDPSQQECVWSHQVLKGTD   80

PcECN   81   VWKKCINCHVAIWNSINSGPGNVHSGLLNSYGCACHAVAHVGYGNPTDGYTACIYFYVPRLSTATPGYFGAKPTLDFRNV   160

PcECN   161   YICFKGTPEGTYTFSGNAPTSLMQLLESKGEVTVKALLVGYDKYANGTVKAKSSAADFLETDFFSALEQAGIFRYEWGTA   240

PcECN   241   SGAVLKNPSVRTHPLTEEAPNGETIVMGVFDIHTGDFILVAPYAPYSRAPYYLPVAVNPGVAACFNCHFVYQGQLGTAKV   320

PcECN   321   MEVGGVWKIGIPADVLNSLTDPHKIVMPAAQAAGGGVAPNLSLVALLATATLLGGAFLALRRRAQ   385

B

C

AcECN   1   MNGGKLALLMVTLAAMGTLVLPSTTS LFLGQHMWYNISGTGNNLPCEKCHADVFAEFKNNPGAHKTIGGGTDTVEHIRAA   80

AcECN   81   CGECHRTSVVGTFASGDGTSATPGQEAHAAATIACMACHEFGPNGNAPYSGAPVAGGFDNVTTDTASSPYNYDNGDTTYG   160

AcECN   161   TKEAHQTFIERAVEDKTLIDSNEACIACHTYVPVKINWTHKVSLEFNCTYEYNTGTSGVTTHYNVTNWTVNGTRYTTVFG   240

AcECN   241   NTTGNGSVNDASNWPGWYPYSW   262

D

Figure S3. Protein sequences and cryo-EM densities of the heme c area in PcECN and AvECN, related to Figure 3

(A) Protein sequence of PcECN. CxxCH or CxCH motifs are highlighted in the cyan shade. The other histidines outside those motifs coordinating heme c are highlighted in green. The predicted signal peptide is in the black dashed line box. The predicted transmembrane region, not seen in the cryo-EM map, is highlighted in red shade.

(B) Zoomed-in views of the heme c area in PcECN. From left to right, heme 1 to heme 4. The protein-heme color scheme remains the same compared with Figure 1. Two cysteines and histidines bound to heme c are also labeled.

(C) Protein sequence of AvECN. CxxCH motifs are highlighted in the cyan shade. The other histidines outside CxxCH motifs coordinating heme c are highlighted in green. The predicted signal peptide is in the black dashed line box.

(D) Zoomed-in views of the heme c area in AvECN. From left to right, heme 1 to heme 4. The protein-heme color scheme remains the same compared with Figure 2. Two cysteines and histidines bound to heme c are also labeled.

A

P. calidifontis ECN

Disulfide bond 1

Disulfide bond 2

Disulfide bond 1

C163

C133

Disulfide bond 2

C62

C69

B

P. calidifontis ECN

C

A. veneficus ECN
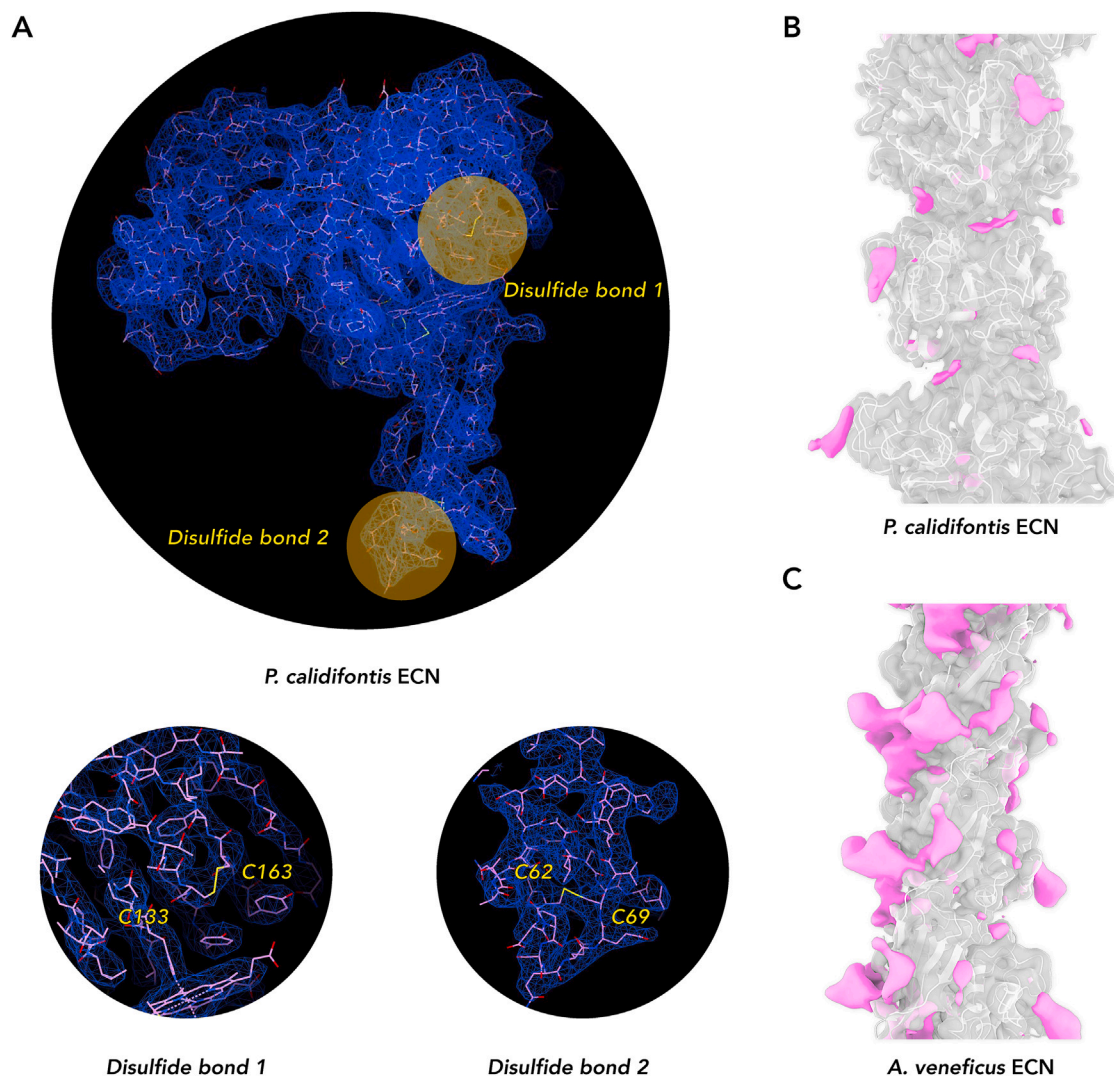
Figure S4. Potential factors contributing to the thermal stability of ECNs, related to Figure 4

(A) Disulfide bonds in *P. calidifontis* ECN. The full atomic model of one *P. calidifontis* ECN subunit is shown on the left with the cryo-EM density corresponding to a single cytochrome subunit. Two disulfide bonds were observed and highlighted in yellow circles. Those two sites are magnified on the right.

(B and C) Surface modifications of PcECN (B) and AvECN (C) filaments. The density accounted for by atomic models is colored in gray, and the extra density is colored in magenta. The protein backbones of ECN filaments are shown in ribbons with protein cryo-EM densities.

Figure S5. *A. veneficus* ECN may have evolutionary link to cytochrome c552, related to Figure 5

(A and B) Results of the HHsearch analysis queried with the sequences of AvECN (A) and AvECN-like protein from a Planctomycetota bacterium (B). The GenBank accession number of (B) is MCH2104266. H(h), α helix; E(e), β strand; C(c), coil.

(C) Heme-based sequence alignment of *A. veneficus* ECN and *T. tepidum* cytochrome c552. Secondary structures are labeled: α helices in rounded rectangles, β sheets in arrows, and loops in dashed lines.

(D) The individual structures of *A. veneficus* ECN, *T. tepidum* cytochrome c552, and their alignment. Four hemes used for the alignments in both structures are highlighted in purple. The unused heme molecular in *T. tepidum* cytochrome c552 is colored orange. Proteins are colored gray.

(E) The individual structures of *A. veneficus* ECN, *T. tepidum* cytochrome c552, and their alignment. Hemes are hidden in this panel. The labeled secondary structures in (C) are colored accordingly. Other unaligned secondary structures are kept gray. A magnified view of the aligned helices is shown on the right.